Neuron

NeuroResource

Ultra-high-density Neuropixels probes improve detection and identification in neuronal recordings

Graphical abstract

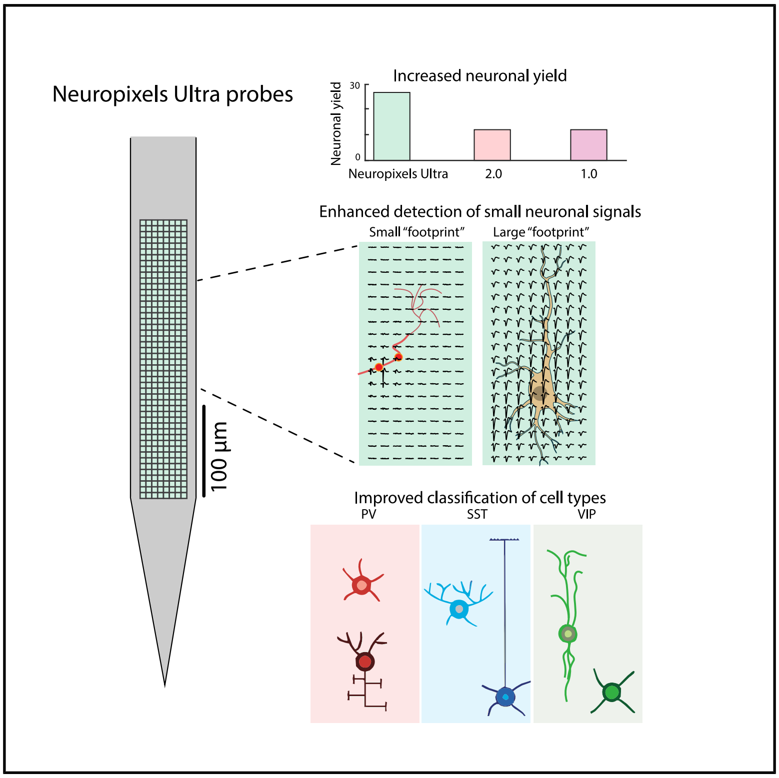

Highlights

- Neuropixels Ultra probes provide ultra-high site density (6 µm site-to-site spacing)
- Higher site density improves the quality and yield of detected neurons
- NP Ultra probes detect waveforms with small spatial "footprints," including axons
- NP Ultra probes improve classification of three types of cortical interneurons

Authors

Zhiwen Ye, Andrew M. Shelton,
Jordan R. Shaker, ..., Shawn R. Olsen,
Timothy D. Harris,
Nicholas A. Steinmetz

Correspondence

nick.steinmetz@gmail.com

In brief

Ye, Shelton, et al. describe a silicon probe with ultra-high site density for recording neural activity in the brain. Higher site density improves the quality and yield of detected neurons. These probes robustly detect extracellular fields with small spatial extents, including axons, across species and brain regions. In addition, these probes improve classification of neuronal cell types.

Ye et al., 2025, Neuron *113*, 3966–3982
December 3, 2025 © 2025 The Author(s). Published by Elsevier Inc.
https://doi.org/10.1016/j.neuron.2025.08.030

CellPress

CellPress
OPEN ACCESS

Neuron

NeuroResource

Ultra-high-density Neuropixels probes improve detection and identification in neuronal recordings

Zhiwen Ye,[1,21] Andrew M. Shelton,[2,3,21] Jordan R. Shaker,[1] Julien Boussard,[4,5] Jennifer Colonell,[6] Daniel Birman,[1] Sahar Manavi,[2] Susu Chen,[6] Charlie Windolf,[4,5] Cole Hurwitz,[4] Han Yu,[4,7] Tomoyuki Namima,[1,8,9,10] Federico Pedraja,[4] Shahaf Weiss,[11] Bogdan C. Raducanu,[12] Torbjørn V. Ness,[13] Xiaoxuan Jia,[14] Giulia Mastroberardino,[15,16] L. Federico Rossi,[17] Matteo Carandini,[15] Michael Häusser,[16,18] Gaute T. Einevoll,[13,19] Gilles Laurent,[11] Nathaniel B. Sawtell,[4] Wyeth Bair,[1,8] Anitha Pasupathy,[1,8] Carolina Mora Lopez,[12] Barundeb Dutta,[12] Liam Paninski,[4,5] Joshua H. Siegle,[3] Christof Koch,[2] Shawn R. Olsen,[2,3] Timothy D. Harris,[6,20] and Nicholas A. Steinmetz[1,22,*]

[1]Department of Neurobiology and Biophysics, University of Washington, Seattle, WA, USA
[2]MindScope Program, Allen Institute, Seattle, WA, USA
[3]Allen Institute for Neural Dynamics, Seattle, WA, USA
[4]Zuckerman Mind Brain Behavior Institute, Columbia University, New York, NY, USA
[5]Department of Statistics, Columbia University, New York, NY, USA
[6]Janelia Research Campus, Ashburn, VA, USA
[7]Department of Electrical Engineering, Columbia University, New York, NY, USA
[8]Washington National Primate Research Center, Seattle, WA, USA
[9]Graduate School of Frontier Biosciences, The University of Osaka, Suita, Japan
[10]Center for Information and Neural Networks (CiNet), National Institute of Information and Communications Technology (NICT), Suita, Japan
[11]Max Planck Institute for Brain Research, Frankfurt, Germany
[12]IMEC, Leuven, Belgium
[13]Department of Physics, Norwegian University of Life Sciences, Ås, Norway
[14]School of Life Sciences & IDG/McGovern Institute for Brain Research, Tsinghua University, Beijing, China
[15]UCL Institute of Ophthalmology, University College London, London, UK
[16]Wolfson Institute for Biomedical Research, University College London, London, UK
[17]Center for Neuroscience and Cognitive Systems, Istituto Italiano di Tecnologia, Rovereto, Italy
[18]School of Biomedical Sciences, The University of Hong Kong, Hong Kong, China
[19]Department of Physics, University of Oslo, Oslo, Norway
[20]Biomedical Engineering Department, Johns Hopkins University, Baltimore, MD, USA
[21]These authors contributed equally
[22]Lead contact
*Correspondence: nick.steinmetz@gmail.com

https://doi.org/10.1016/j.neuron.2025.08.030

SUMMARY

To understand the neural basis of behavior, it is essential to sensitively and accurately measure neural activity at single-neuron and single-spike resolution. Extracellular electrophysiology delivers this, but it has biases in the neurons it detects and it imperfectly resolves their action potentials. To minimize these limitations, we developed a silicon probe with much smaller and denser recording sites than previous designs, called Neuropixels Ultra (NP Ultra). Using NP Ultra, neuronal yield in mouse visual cortex recordings increased by more than 2-fold. With ultra-high spatial resolution, we discovered that a feature of extracellular waveforms, the spatial extent or "footprint," distinguished axonal from somatic recordings. In addition, three genetically identified cortical cell types could be discriminated from one another with ~80% accuracy and from other neurons with ~85% accuracy. NP Ultra improves yield, detection of subcellular compartments, and cell type identification to enable a more powerful dissection of neural circuit activity during behavior.

INTRODUCTION

High-density silicon electrode arrays, such as Neuropixels probes, have enabled prolonged recordings of hundreds to thousands of neurons across many brain regions in a single experiment.[1–3] Their versatility and robustness have enabled collection of these datasets in diverse species, including fish, rodents, monkeys, reptiles, and humans.[4–10] The use of Neuropixels has driven discoveries and insights into the nature of decision-making, perception, and the brain-wide dynamics of neuronal processing.[4,7,11–18]

Despite these successes, key technical challenges remain. First, the spatial resolution of previous generations of Neuropixels probes is relatively low: the nearest contact-to-contact spacing is ∼25 μm in Neuropixels 1.0 (NP 1.0) and ∼15 μm in 2.0 (NP 2.0). Accordingly, previous probes cannot optimally sample fine-scale brain structures, such as small nuclei or thin cell layers, and have limited ability to finely resolve electrical fields of individual neurons. Although our knowledge of electrical fields at the columnar level and beyond, such as the local field potential (LFP) and electroencephalography (EEG), is extensive,[19–23] we have been unable to access electrical fields at the micrometer scale. Moreover, the low density of previous probes may undersample extracellular action potentials with electrical "footprints" (i.e., the detectable spatial extent of the extracellular action potential) smaller than the span between electrode contacts, potentially creating a sampling bias against such small-footprint signals.

In addition, the brain contains a large diversity of cell types, and extracellular electrophysiology has been limited in its ability to discriminate between these types.[24,25] Classically, extracellularly recorded neurons in some brain regions, such as the cortex and striatum, have been separated into coarse cell types on the basis of features such as waveform shape and firing pattern.[26–36] NP 1.0 probes can provide additional coarse morphological information about the electrical field surrounding a neuron useful for neuron classification,[36–38] but this information may not be detailed enough to resolve the large diversity of cell types in the brain. The possibility that higher-resolution electrode arrays could improve cell type classification remains largely unexplored.

We hypothesized that a probe with increased sampling density would address each of the above technical challenges by accessing electrical field microstructures. Here, we describe "Neuropixels Ultra" (NP Ultra), a probe with substantially smaller and denser recording sites than previous probes. NP Ultra is effectively an implantable voltage-sensing camera that captures a planar image of a neuron's electrical field. This probe exhibits improved yield, detection, and cell type classification of neurons and processes across brain regions and species.

RESULTS

Probe design and characterization

We designed a new version of the Neuropixels probe with substantially smaller and denser recording sites, called NP Ultra. The probe has 5 × 5 μm titanium nitride (TiN) recording sites on a 768 × 8 grid with 1 μm gaps (for 6 μm center-to-center spacing), densely sampling a 4.6 mm × 48 μm span of brain tissue (Figures 1A–1D). The site size and spacing compare favorably with NP 1.0 probes (12 × 12 μm electrodes and 20 × 16 μm staggered spacing). The probe form factor (shank dimensions and probe base) is identical to NP 1.0, as are its mechanical characteristics. Like existing NP 1.0 and 2.0 probes,[1,3] NP Ultra records from 384 channels simultaneously out of the 6,144 total available sites. NP Ultra features switchable recording sites with multiple configurations, including 48 × 8 for maximum density, along with 96 × 4, 192 × 2, and 384 × 1 site arrangements for longer spans at reduced density (Figures 1E and S1). This flexibility is achieved using a grouped switching arrangement in which multiple sites share switch memory due to space constraints. These configurations can be selected at various positions along the ∼4.6-mm total site span. NP Ultra's substantially higher site density provides much higher spatial resolution of extracellular voltages compared with lower-density probes (Figures 1B–1E), while sacrificing recording span. Recording individual neurons *in vivo* with this device revealed detailed portraits of their extracellular action potentials (Figure 1H).

NP Ultra's smaller recording sites have larger electrical impedance and, accordingly, slightly larger per-channel noise levels, as predicted,[39] but otherwise retain the uniform gain, low crosstalk, and low light sensitivity of other Neuropixels probes. In self-referenced noise measurements of NP 1.0 and NP Ultra probes in saline, we observe a small but significant difference in root-mean-square (RMS) noise (Figure 1G; 0.26 μV; 95% confidence interval from t test = 0.19–0.34 μV). Estimating noise within tissue is complicated by the presence of true biological signals, which typically far exceed electrode noise. We obtain an approximation by selecting sites with low activity levels and estimating the noise with the median absolute deviation, which is less sensitive to outliers than RMS.[40] We found that noise levels *in vivo* were 20% ± 2% higher for NP Ultra than for NP 1.0 (Figure 1G; NP 1.0: 10.5 μV *in vivo*; NP Ultra: 12.67 μV; difference = 2.1 μV; 95% confidence interval from t test = 2.0–2.3 μV). The difference in noise between NP Ultra and 1.0, and the difference between saline and *in vivo* measurements, is well captured by a noise model incorporating the properties of TiN electrodes and probe electronics, with higher impedance *in vivo* and a contribution of background neural activity (Figure S1; see STAR Methods). Though per-site noise levels are higher for these probes, we found that they nevertheless have highly uniform channel-to-channel gain, negligible crosstalk, and no larger light sensitivity than probes with larger sites (Figure S1). Recordings of LFPs were similar to probes with larger sites (Figure S2).

Higher site density improves the quality and yield of spike sorting

We reasoned that a probe with 10-fold higher site density would provide improved data quality despite slightly higher per-channel noise levels, as it would sample individual action potentials at more recording sites. This could lead to higher peak waveform amplitudes, higher signal-to-noise ratio (SNR) for each waveform, improved spatial localization of waveforms, and improved ability to stably record neurons during relative probe-brain motion.

We applied a new spike-sorting algorithm, DARTsort,[41] which is well suited to dense recordings. The algorithm, described in detail in the STAR Methods and demonstrated on simulated data in separate work,[41] relies on estimating the 3D spatial location of each spike relative to the probe using a point-source model.[42] We use these locations to infer the motion of the probe relative to the brain over time,[43] register the spike positions, and cluster the spikes (Figures 2A and 2B), which provides an accurate approximation of waveform shapes across probe motion, demonstrated by small residuals (Figures 2C, 2D, and S3). Using this sorting algorithm, we automatically sorted about one

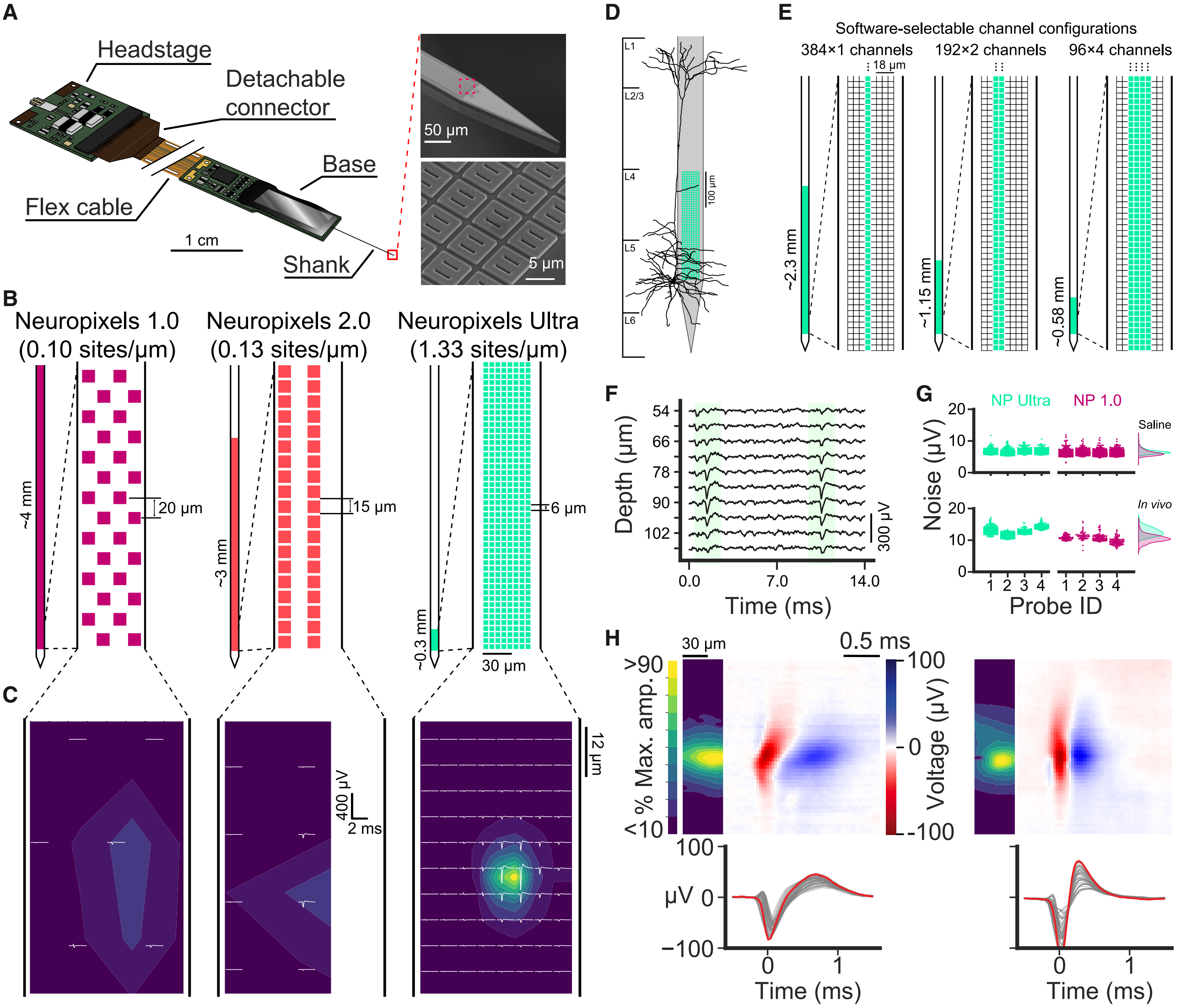

Figure 1. NP Ultra probes have a denser site layout but smaller span compared with NP 1.0 and 2.0

(A) Left: schematic of a complete NP Ultra probe. Right: scanning electron microscope images of an NP Ultra probe tip (top) and individual contacts (bottom).

(B) Layout of NP Ultra sites compared with previous probes.

(C) Comparison of an example waveform on all three probes. The example NP Ultra waveform (right) was spatially re-sampled to estimate its appearance on the NP 1.0 (left) and NP 2.0 (middle) site configurations. Heatmaps represent the interpolated voltage normalized to peak amplitude in the NP Ultra configuration.

(D) Scale of a mouse L5 pyramidal neuron from the Allen Institute Cell Types Database compared with an NP Ultra probe.

(E) Schematics of span and site layout for various probe configurations.

(F) Example raw traces from a column of vertically adjacent recording sites, with two spikes (shaded).

(G) Measures of noise in saline (top, root mean square) and during recording *in vivo* (bottom, median absolute deviation).

(H) Example spatial (top left), spatiotemporal (top right; from the column of sites containing the peak), and temporal (bottom; peak [red] with 40 nearby channels [gray]) waveforms recorded by NP Ultra from a regular spiking (left) and a narrow spiking (right) neuron in the visual cortex of an awake mouse.

See also Figures S1 and S2 and the signal attenuation, saline noise, and brain noise tables in the STAR Methods.

hundred neurons from recordings with NP Ultra probes in the mouse visual cortex (147 ± 37 total neurons per recording, 44 ± 22 neurons with reliable visual responses, mean ± SD, n = 10 recordings).

Spikes recorded with NP Ultra probes have higher peak waveform amplitudes, higher SNRs, and more precise spatial estimates of spike locations than those recorded with previous Neuropixels probes due to the increased spatial sampling. To measure this, we spatially resampled our NP Ultra recordings to simulate the signals that would have been recorded from the exact same position under different recording site patterns: an NP 1.0-like pattern; an NP 2.0-like pattern; and a hypothetical "large-dense" pattern with large 12 × 12 µm recording sites, as in NP 1.0 and 2.0, but with dense, gapless spacing as in NP

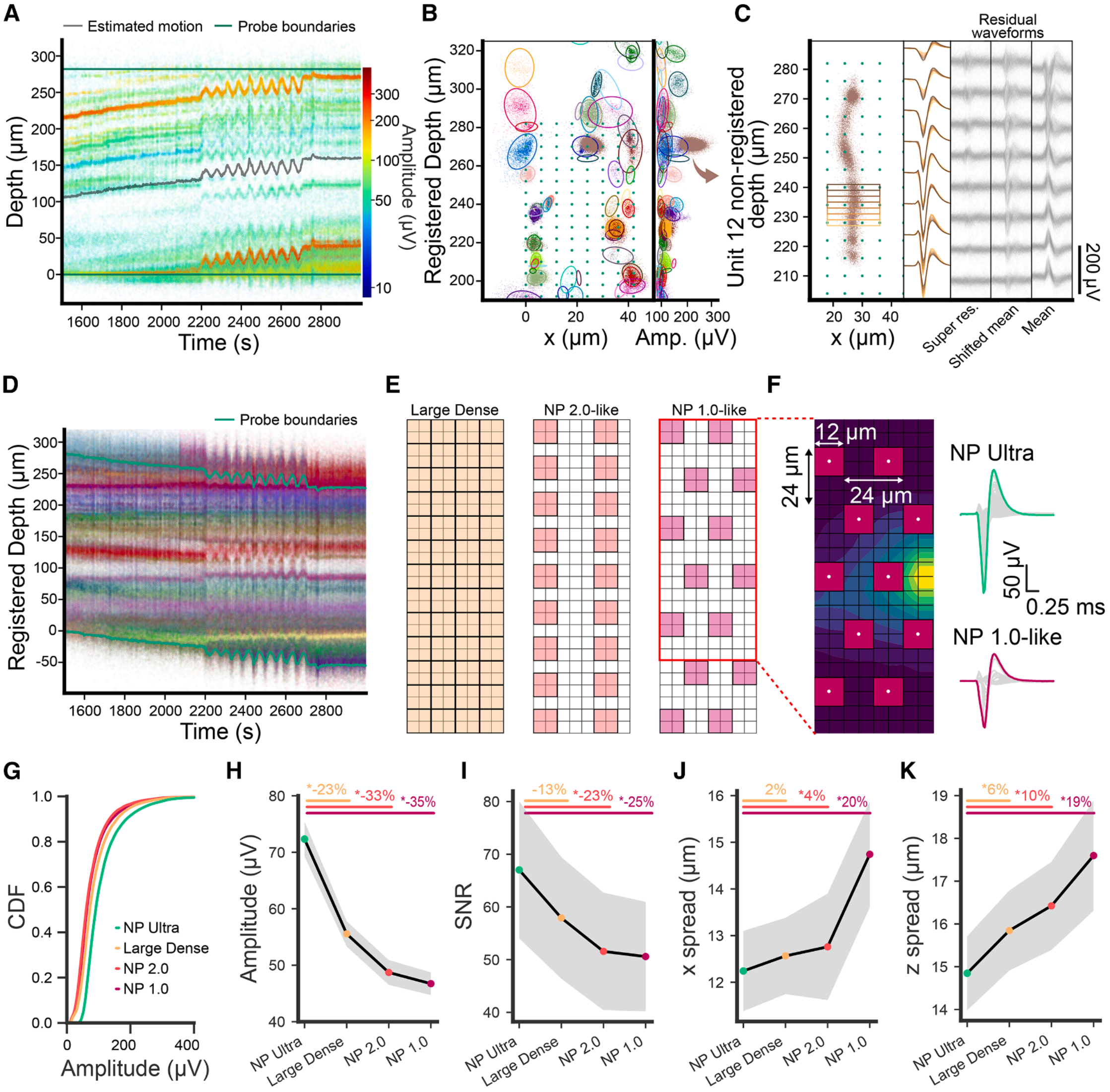

Figure 2. Localizing, clustering, and tracking spikes from NP Ultra probes

(A) “Drift map” spatial spike raster of detected neurons in an example recording. Each point represents one spike.

(B) Registered spike locations and amplitudes. Left: each spike’s fitted source coordinate in registered 2D space, colored by cluster identity, with ellipses representing each cluster’s spatial spread. Green, recording site locations. Right: scatter of depth vs. spike amplitude.

(C) Super-resolution template waveform and fit quality for cluster 12. Left: non-registered spike positions. Colored rectangles indicate spikes used for estimating each component of the super-resolution template. Middle: super-resolved templates for cluster 12 overlaid. Right: residual waveforms obtained after subtracting the super-resolution templates shifted according to the estimated motion, the mean template when shifted, and the un-shifted mean template.

(D) Drift map as in (A), post-motion registration. Spikes colored by their cluster identity.

(E) Three spatial resampling patterns (large-dense, NP 2.0-like, and NP 1.0-like patterns, from left to right).

(F) Left: grid indicating the NP Ultra recording channels (black) and the NP 1.0-like resampled sites (magenta squares). Colormap indicates amplitude as in Figure 1C. The corresponding NP Ultra and resampled waveforms are shown on the right, with all channels overlaid and the main channel colored.

(G) Cumulative distribution function of all spike amplitudes, comparing different site arrangements.

(H) Peak site amplitudes of neurons in the original dataset recorded with NP Ultra vs. the spatially resampled versions. Error shading represents SEM. * indicates statistical significance of the difference, (two-sample z test).

(I) Template SNR for each recording site pattern.

(J) Spatial spread, computed as the standard deviation of coordinates, in the horizontal dimension.

(K) Spatial spread in depth.

See also Figures S3–S6.

Ultra (Figures 2E and 2F). This computational resampling strategy produces datasets exactly matched in terms of the spiking events present, differing only in the sampling density, thus permitting us to directly compare the properties of the signal as observed with NP Ultra with what would have been observed with other, less-dense probes. This strategy enables comparison of the recording properties of each probe without being confounded by the substantial session-to-session variability found in real recordings.[44]

Peak spike amplitudes were highest in the original NP Ultra recording (Figures 2G and 2H). Reductions in peak site amplitude observed on the large-dense pattern (23% difference) reflect the effect of larger recording sites relative to NP Ultra, while reductions in amplitude under the 1.0-like (35% difference) and 2.0-like (33% difference) site patterns reflect the effect of larger sites averaging across space[45–47] in addition to a failure to sample the peak location due to gaps between sites[48] (Figures S4 and S5).

The higher amplitude of spikes measured with NP Ultra (Figures 2G and 2H) overcomes the higher noise of its small sites (Figure 1G), resulting in higher SNR when considering the combined signal recorded across all channels. We computed a "template SNR" for each neuron (see STAR Methods and Figure 2I). Neurons recorded with NP Ultra had the greatest template SNR, followed by the large-dense, 2.0-like, and 1.0-like site patterns, in that order (Figure 2I). As with amplitude, the magnitude of the effect varies across brain regions, depending on the distribution of waveform footprint (Figure S4). Our data moreover suggest that an intermediate site size with minimal gaps between sites may comprise an optimal site layout for most neurons in most mouse brain regions (Figure S5).

The increased recording site density of NP Ultra also produced substantially greater precision in the estimated spatial position of each spike relative to previous probes (Figures 2J and 2K). The success of the spike-sorting strategy described above depends on the ability to spatially segregate spikes from individual neurons relative to nearby neurons. Spike locations were estimated with substantially higher precision in the NP Ultra dataset (Figures 2J, 2K, and S6), confirming that these probes are well suited to employ this spike-localization-based sorting strategy.

The improved SNR and spatial precision increased yield of sortable neurons. We evaluated yield by focusing on neurons that were present throughout the recording and had reliable and selective responses to visual stimuli (see STAR Methods and Figures 3A, 3B, and S7A). We found that NP Ultra had a higher yield of visually responsive neurons, with over 10 extra neurons on average than the 1.0-like, 2.0-like, and large-dense patterns (Figures 3C–3E). The large difference in yield between Ultra and 1.0 amounted to a greater than 2-fold improvement. NP Ultra recorded from more neurons with both large and small amplitude waveforms (Figure 3E). When further filtering neurons for those meeting strict quality metrics[18] (see STAR Methods), the yield differences between NP Ultra and resampled patterns are relatively smaller, though NP Ultra still improved the yield of these well-isolated single neurons (1.7× greater yield of NP Ultra relative to 1.0-like on average; Figures 3C and 3D).

The increased yield of visually responsive neurons from NP Ultra translated into a higher performance decoding of visual stimuli. The accuracy of decoding image identity was significantly higher for NP Ultra than the large-dense, 2.0-like, and 1.0-like patterns (Figure 3F; 1.8%, 3.8%, and 3.0% respective increase in median accuracy across sessions; $p = 0.016$, 0.008, 0.008, signed-rank test). The increase in decoding accuracy for NP Ultra resulted from an increased number of neurons rather than any difference in properties of recovered neurons, as decoding accuracies were equal when the number of included neurons was matched between patterns (Figure 3G). Further analyses revealed that neurons with low-amplitude waveforms, as recorded more successfully by NP Ultra, had significant visually decodable information (Figures S7E–S7G).

The higher site density of NP Ultra also afforded a moderately improved ability to stably track drifting neuron locations across time. To measure this, we imposed slow probe motion as a ground-truth pattern of unstable probe location relative to the brain during the visual fingerprint sessions.[3] We then computed a stability ratio for each visually responsive neuron by comparing pre- and post-motion visual responses, where a ratio of 1 indicates perfect stability (see STAR Methods and Figures S7B–S7D). We found that there was a significant but modest difference in stability ratio between NP Ultra, 1.0-like, and 2.0-like patterns but not between NP Ultra and the large-dense pattern (% difference between Ultra and large-dense, 2.0-like, and 1.0-like = 11.4%, 18.3%, and 15.1%, respectively; $p =$ 0.062, 0.0030, 0.0064, Mann-Whitney U test) (Figure 3H).

Subcellular recordings from axons and dendrites in mouse isocortex

Neurons or subcellular structures with waveforms that decay over distances smaller than 20 μm would not be detected by NP 1.0 probes if an action potential was initiated between electrode contacts, but they were observed in our dataset (Figure 4A). To quantify this observation, for each waveform, we calculated its "spatial footprint" as the radius from the peak channel at which the average spike amplitude fell below 30 μV, a value sufficiently above the noise level (Figures S8A–S8C). We observed a bimodal distribution of this quantity, with a substantial fraction of footprints less than 20 μm, which we define as having a "small footprint" (Figure 4B).

Small-footprint waveforms likely originated from axons. To test this, we applied the GABA agonist muscimol to the cortex to suppress somatic spiking while leaving the activity of non-local axons unaffected. All recorded waveforms that survived muscimol application (firing rate > 1 spike/s in muscimol; 23/175, $n = 6$ sessions, $n = 3$ mice) had a small footprint (Figures 4C–4G). Not all small-footprint waveforms survived muscimol application, which is consistent with recordings from axons of local origin. Aside from their small spatial footprint, the muscimol-resistant axonal waveforms were inconsistent in appearance: some had narrow, negative peaks with little or no early positive component, while others had prominent early positive peaks (Figures 4G and S9). Similarly, spike waveforms histologically localized to the corpus callosum could have either or both of these waveform characteristics (Figures S10A–S10C). Biophysical simulations confirmed that small-footprint, narrow negative spikes could be observed at nodes of Ranvier[23] (Figure S10D), that positive peaks may arise in unmyelinated segments of otherwise myelinated axons

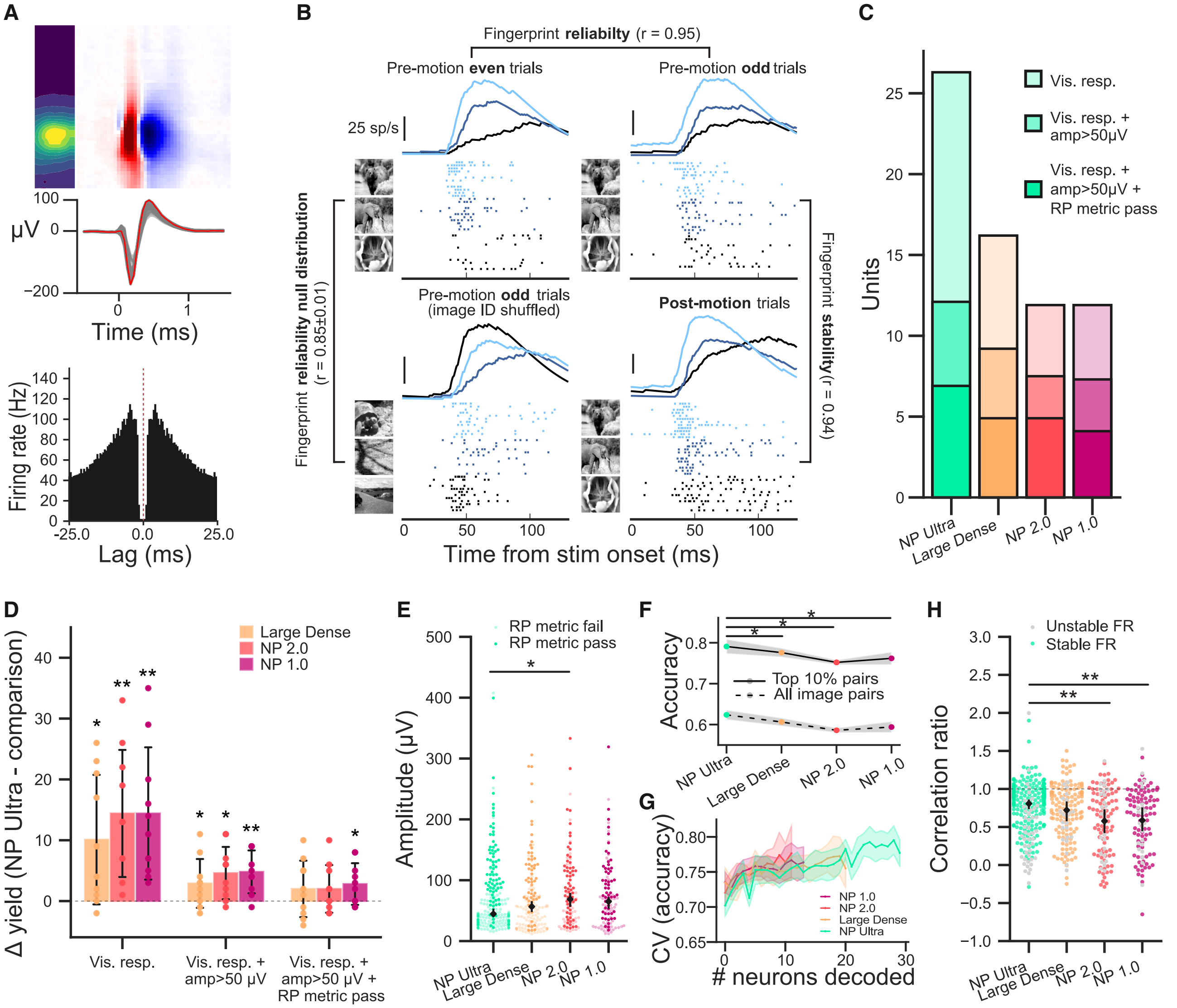

Figure 3. NP Ultra increases neuron yield and tracking stability

(A) Waveform (top, as in Figure 1H) and autocorrelogram (bottom) for an example neuron.

(B) Peri-stimulus spike rasters and firing rates for example neuron from (A) to three example images, showing similar visual responses within pre-motion trials (“fingerprint reliability”) and between pre- and post-motion trials (“stability”) against a shuffled control (bottom left).

(C) Mean neuronal yield across sessions, progressively filtered by reliable visual response (“vis. resp.”), spike amplitude >50 µV, and a refractory period quality metric (“RP metric pass”).

(D) Per-session differences in neuron yield between NP Ultra and resampled patterns. *$p < 0.05$; **$p < 0.01$ (Wilcoxon signed-rank test).

(E) Amplitude distributions of visually responsive neurons. Diamonds are medians with 95% confidence intervals (CIs). *$p < 0.05$ (Mann-Whitney U test).

(F) Median decoding accuracies ($n = 10$ sessions) for all image pairs and for the top 10% of the most decodable pairs. *$p < 0.05$ (Wilcoxon signed-rank test).

(G) Median decoding accuracy (top 10% most decodable pairs) vs. number of neurons included.

(H) Stability ratios for visually responsive neurons. **$p < 0.01$ (Mann-Whitney U test).

See also Figure S7.

(Figure S10E), and that unmyelinated axons are unlikely to be detected, given their small amplitude, except when they have substantial branching and termination[49] (Figure S10E). Therefore, the characteristics of axonal spikes vary dramatically depending on the exact properties of the axon recorded but are unified by their small spatial footprint rather than any particular waveform-peak direction, number, or width.

NP Ultra also records from dendritic compartments of neurons with higher resolution and SNR than previous technologies. Extracellular recordings of back-propagating action potentials in apical dendrites of cortical pyramidal neurons have been reported with NP 1.0[38] and with other probes.[50] We made recordings with NP Ultra and NP 1.0 using an insertion strategy to obtain recordings in mouse V1 approximately aligned with apical

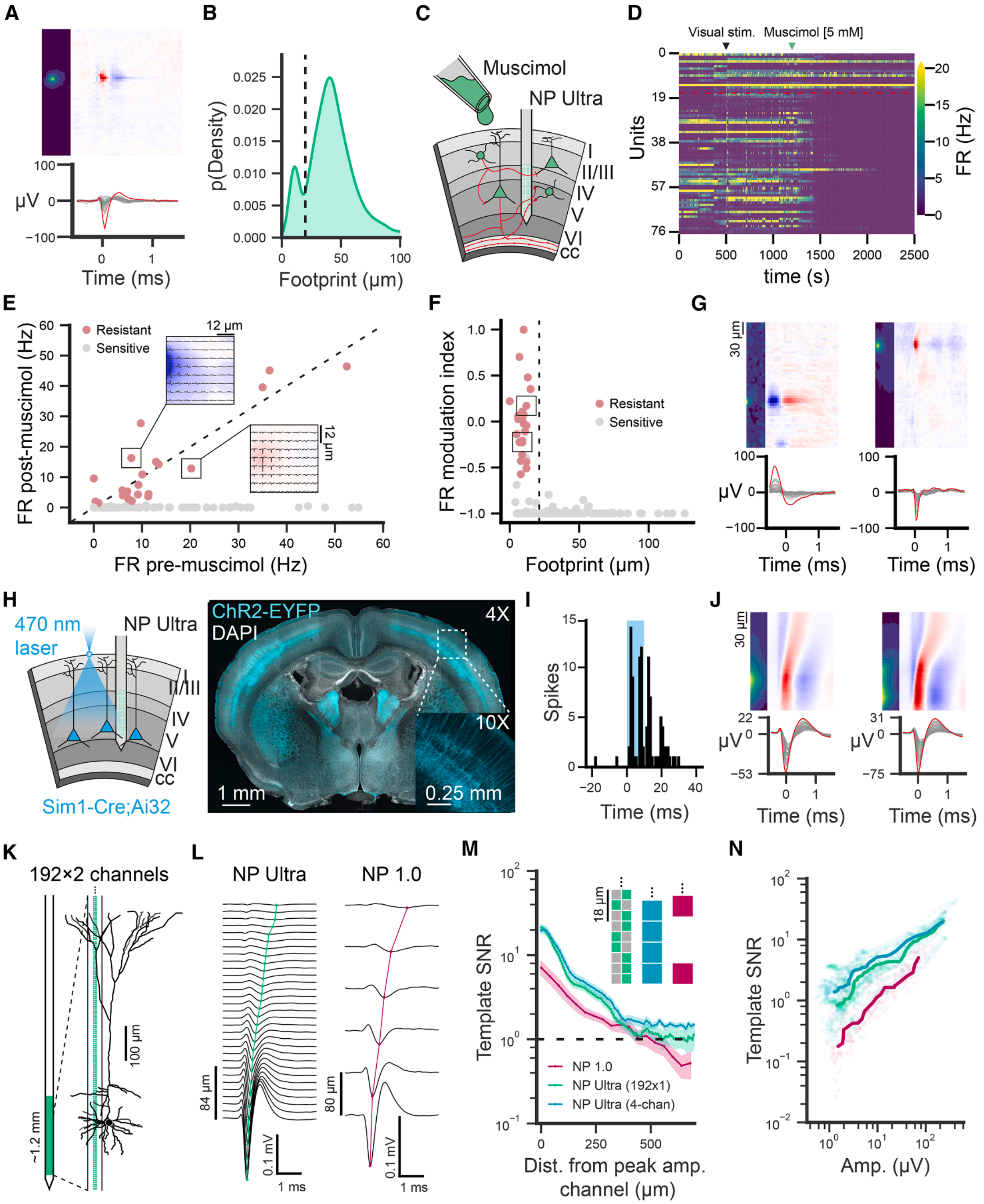

Figure 4. Recordings from subcellular compartments

(A) Example small-footprint waveform recorded from VISp.

(B) Histogram of measured spatial footprints across a total of 175 units recorded in the mouse visual cortex with muscimol application (*n* = 3 mice, 6 sessions). Dashed line, threshold of small footprint (20 μm).

(C) Schematic of NP Ultra recordings in the cortex with surface application of muscimol. Red lines, axonal segments.

(D) Firing rates for an example recording. Units sorted by ascending footprint size. Red line, threshold of small footprint.

(E) Scatterplot of firing rates pre- and post-muscimol application. Dashed line, identity. Insets: small-footprint waveforms of two example units.

(F) Relationship between the spatial footprint and firing rate modulation index. Black boxes, units from (E).

(G) Full waveforms of the two units marked in (E).

(H) Left: schematic of optotagging experiment in Sim1-Cre;Ai32+ L5b pyramidal neurons. Right: histology showing labeled L5 pyramidal neurons.

(I) Peri-stimulus time histogram (PSTH) of an example Sim1+ unit in response to photostimulation.

(legend continued on next page)

dendrites. First, we optotagged layer 5 pyramidal neurons (Figures 4H and 4I; Sim1-Cre;Ai32) and observed propagation in waveforms consistent with known back-propagation waveform characteristics (i.e., initial positive peak at the time of the somatic spike[51]) and speed[52] (Figure 4J). Then, to record dendritic signals across a larger extent of the apical tree, we switched to the linear 192 × 2 configuration (Figures 4K and 4L). With this configuration, we recorded back-propagation dynamics spanning more than 400 μm from the putative somatic channel, at ~7× higher spatial resolution than with NP 1.0 (6 μm linear spacing vs. 40 μm; Figure 4L). This enhanced resolution led to significantly greater SNR in resolving back-propagating signals across the apical dendrite (Figures 4M and S8D–S8F). These improvements over NP 1.0 recordings did not depend on probe alignment or recording quality, as they persisted when comparing dendritic signals of similar amplitudes (Figure 4N). In addition to back-propagation, our dataset revealed a number of distinctive waveforms with spatiotemporal characteristics not previously reported, which appear similar to biophysical simulations of close dendritic apposition (Figure S11). Taken together, NP Ultra enables subcellular recordings from dendrites with improved resolution and SNR relative to prior devices.

Small-footprint extracellular action potentials across mouse brain regions and different species

To assess the prevalence of small-footprint action potentials across different brain regions and species, which may be undersampled with previous electrophysiological probes (Figure S12), we made NP Ultra recordings in multiple brain regions within the mouse brain and specific brain regions in multiple species.

We recorded 4,666 single units in 18 brain regions in the awake head-fixed mouse brain (>50 single units/region; $n = 4$ mice; $n = 12$ sessions; Figure 5A). NP Ultra recorded many small-footprint waveforms in each brain region with a range of diverse spatial features (Figure S13), reflecting otherwise unobservable or undersampled units. As in NP 1.0 recordings,[38] we observed a wide distribution of single-channel spike waveform features, such as amplitude, peak-to-trough ratio (PTR), and spike duration, across brain regions (Figure S14). In each brain region we recorded, a significant fraction of extracellular action potentials (>10% in most regions) had a spatial footprint of less than 20 μm (Figures 5B and 5C). This fraction of small-footprint waveforms was significantly greater in recordings localized to the corpus callosum (57.5%, 31.4 ± 26.1 μm, mean ± SD, 113 units) and the dentate gyrus (DG) (75.3%, 20.0 ± 16.2 μm, 77 units) compared with the primary visual cortex (VISp), for example (10.0%, 50.0 ± 25.6 μm, 359 units; Figure S15). These small-footprint units may reflect recordings from axons or from neurons with exceptionally small somata, such as granule cells in DG, or both.

We observed a substantial number of units with a footprint of less than 20 μm in each of the four species, establishing the generality of this observation (Figures 5D–5G). We found 13/124 small-footprint waveforms (10.5%) from the monkey visual cortex, closely matching the mouse (36/359, 10.0%). The similar overall distribution of footprints between mouse and monkey visual cortex is consistent with the similar distribution of somatic sizes in this area across these two species, despite differences in soma size in other cortical regions.[53] A similar proportion of units in the lizard medial cortex had small footprints (2/19, 10.5%). Close to half of the units detected in the cerebellum (CB) of the electric fish had small footprints (18/37, 48.7%). Together, these observations demonstrate that units with small spatial footprints (<20 μm), which are difficult to detect with lower-density probes, are consistently detected with NP Ultra across species.

Spatial footprints of genetically identified cell types

In addition to dependence on subcellular morphology and brain region as described above, the spatial footprint of recorded neurons differed between genetic cell types. To measure and compare the spike waveforms of genetically identified cells, we performed optotagging of three inhibitory neuron types[54] in the visual cortex: parvalbumin- (PV), somatostatin- (SST), and vasointestinal polypeptide (VIP)-expressing cells (Figures 6A and 6B). 243 PV, 116 SST, and 126 VIP interneurons were identified as optotagged based on both unsupervised density-based clustering methods and qualitative assessment (243/3,344 = 7.3% of units tagged in PV-targeting mice; 116/2,641 = 4.4% for SST; 126/3,492 = 3.6% for VIP; Figures 6B–6D and S16; STAR Methods). Optotagged neurons had diverse spatiotemporal waveforms (Figures 6C and S16; Video S1). We computed the spatial footprint of each optotagged unit and found that footprints were predominantly large and significantly differed across all three cell types (Figure 6D; $p < 0.001$, Kruskal-Wallis; median footprint = 40.0 μm for PV, 35.0 μm for SST, and 42.0 μm for VIP; $p = 0.01$, PV vs. SST, ranksum; $p = 0.01$, PV vs. VIP; $p < 0.001$, SST vs. VIP).

We separated all untagged units into narrow spiking (NS, duration < 0.4 ms; $n = 2{,}058$) and regular spiking (RS, duration ≥ 0.4 ms; $n = 6{,}838$) based on spike duration and examined footprint distribution within these two groups (Figures 6E and 6F). Surprisingly, we found that NS waveforms displayed a distinctly bimodal footprint distribution compared with RS. Based on this observation, we subdivided the untagged NS group into two categories based on their footprint (greater or less than 20 μm), which we call large NS (NS_L, $n = 952$) and small NS (NS_S, $n = 1{,}133$) units. PV+ optotagged neurons had an overlapping

---

(J) Two example Sim1+ waveforms with visible propagation (diagonal red band).
(K) Schematic of an L5 neuron recorded with the linearized (192 × 2) configuration.
(L) Example bAPs recorded with NP Ultra (left) and NP 1.0 (right). Traces show spike-triggered average waveforms ($n = 2{,}000$ spikes) recorded from the column of channels that includes the peak amplitude channel. Colored traces, voltage minima.
(M) Template SNR as a function of vertical distance from the peak amplitude channel for NP Ultra (192 × 2 configuration, best column selected, green), NP Ultra (192 × 2 configuration, 4-channel average, teal), and NP 1.0 probes (magenta).
(N) Template SNR against amplitude.
See also Figures S8–S11.

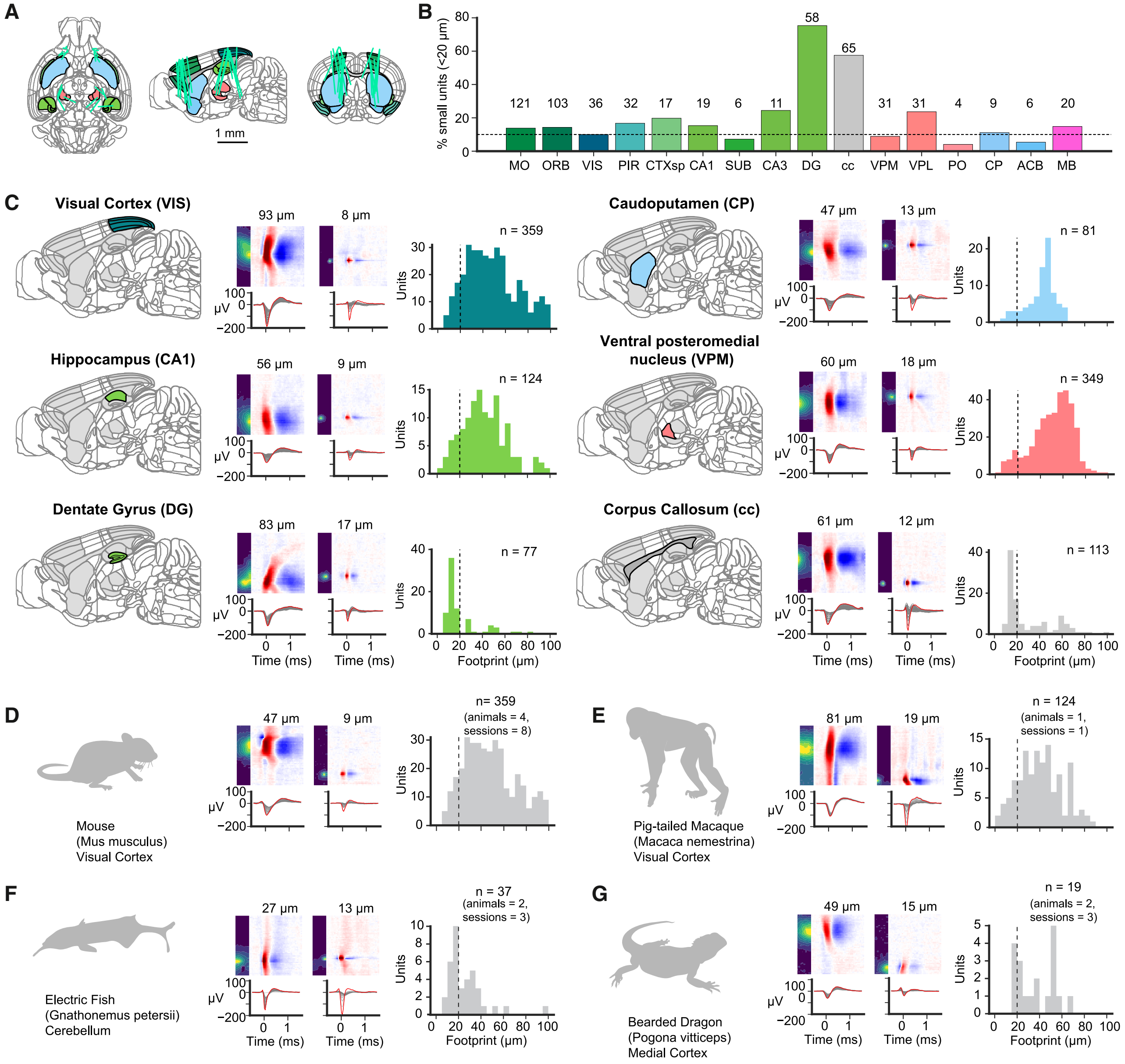

Figure 5. NP Ultra recordings reveal small electrical footprint units in many brain regions of the mouse and across different species

(A) NP Ultra insertion trajectories.

(B) Percentage of units with small footprints less than 20 µm in example mouse brain regions. The number of small units per region is indicated.

(C) Example waveforms (one large and one small footprint) from each of six brain regions, and spatial footprint histogram from these regions. See https://npultra.steinmetzlab.net/ for a browsable interface to explore this dataset.

(D) Same as (C) but for the mouse visual cortex.

(E) Same as (C) but for the monkey visual cortex.

(F) Same as (C) but for the electric fish CB.

(G) Same as (C) but for the bearded dragon medial cortex.

Region abbreviations, see STAR Methods.

See also Figures S12–S15.

distribution of footprint with NS_L but not with NS_S (Figure 6G). In addition, PV+ neurons and NS_L units were not well discriminable, with multiple waveform features (see STAR Methods) using linear discriminant analysis (0.56 ± 0.04, mean ± SEM), whereas PV+ neurons and NS_S units were highly discriminable (PV:NS_S, 0.87 ± 0.02; Figure 6H).

NS_S provided either excitatory or inhibitory monosynaptic input to putative downstream neurons, further supporting the

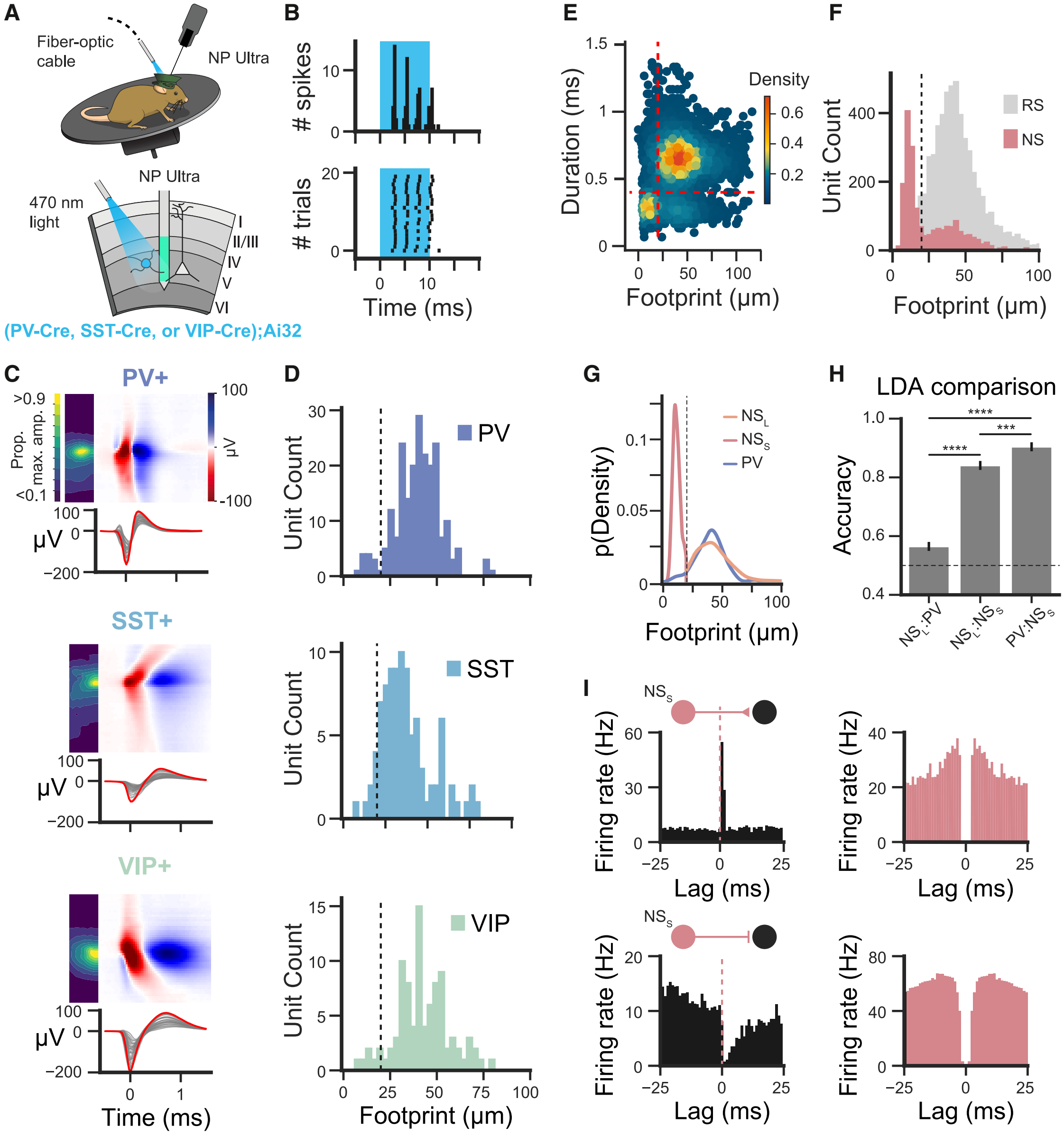

Figure 6. Optotagging three inhibitory neuron classes measured with NP Ultra

(A) Schematic of experimental setup. Visual cortical neurons transgenically expressing channelrhodopsin were recorded with NP Ultra probes and optotagged using 470 nm light.

(B) Light-driven responses of an example PV-Cre;Ai32-expressing unit during a 10 ms pulse.

(C) Example waveforms from optotagged units in each mouse line.

(D) Distributions of spatial footprints for each line.

(E) Scatterplot of waveform duration and footprint size, colored by the local density of points.

(F) Distributions of footprints for all units, segregated by waveform duration dashed line, footprint threshold (20 μm).

(G) Comparison of footprint distributions between PV and NS units.

(H) Accuracy of linear discriminant analysis (LDA) in separating different types of NS and PV units using pre-peak-to-trough ratio (prePTR) and PTR as features.

(I) Left: cross-correlograms of example pairs that include an NS$_S$ unit. Right: autocorrelograms of the example NS$_S$ units.

See also Figures S16 and S17.

interpretation that, despite their NS waveform, they arise from axonal recordings rather than PV+ interneurons. To investigate this, we performed an analysis of cross-correlograms to identify putatively monosynaptically connected pairs. Such pairs were extremely rare (<0.02% of all observed interactions, >125,000 pair interactions; Figures 6I and S17). We found instances of both putative excitatory and inhibitory interactions at short latencies (<3 ms) from the time of an NS$_S$ unit. In recordings with

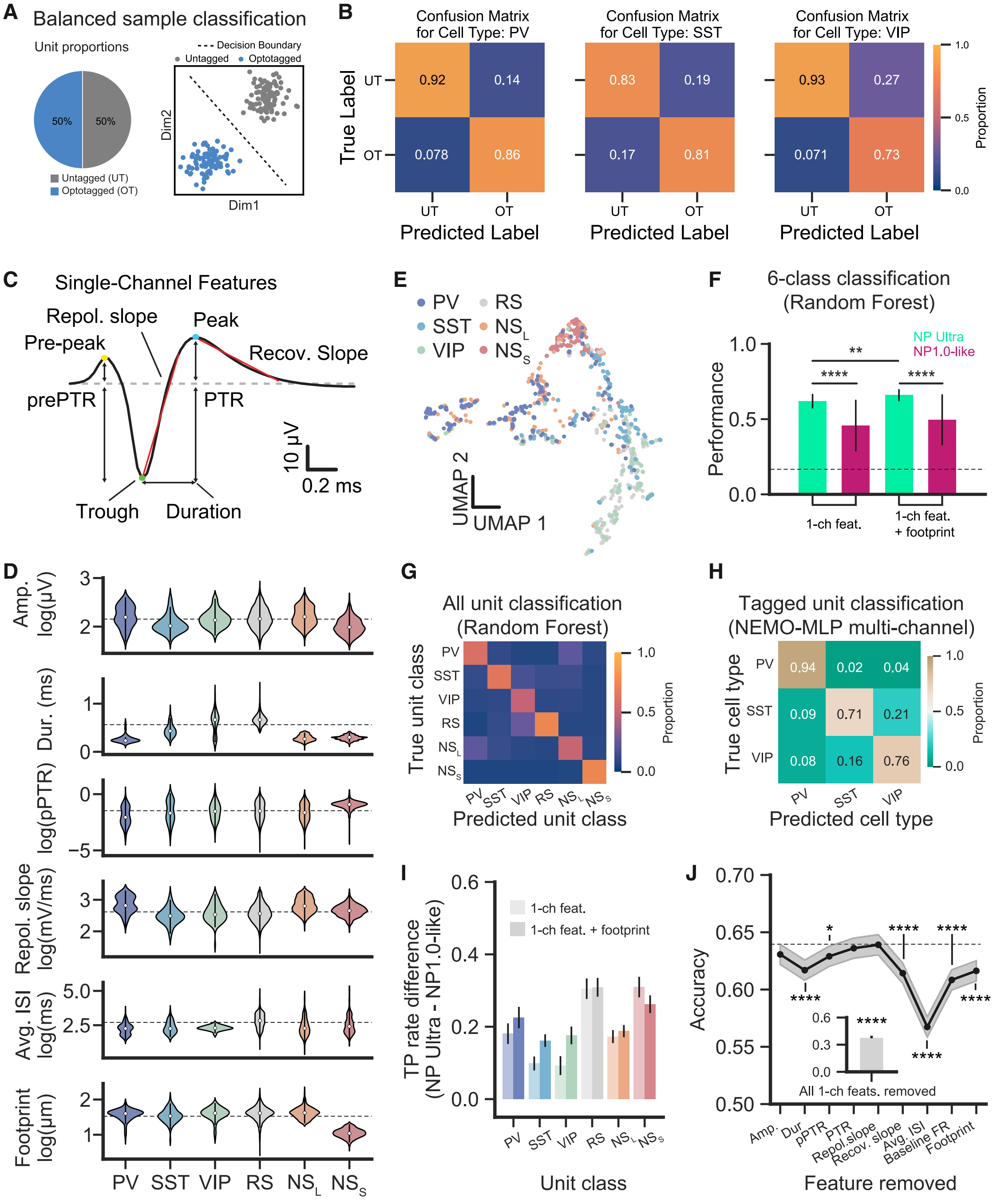

Figure 7. Enhanced classification of inhibitory neuron types with NP Ultra

(A) Schematic of the classification scheme using balanced unit proportions and a logistic regression classifier with all features included.

(B) Confusion matrices for each interneuron type classified.

(C) Schematic of features extracted from single-channel waveform (“1-ch features”). Red lines show slopes for repolarization and recovery.

(D) Distributions of waveform features for each type of neuron. Dots, median; black vertical lines, interquartile range. Dashed horizontal lines, population median.

(E) Uniform manifold approximation and projection (UMAP) of an equally sampled subset of NP Ultra-recorded units from each unit class.

(F) Classifier performance (out-of-bag score, mean ± SD) on NP Ultra (green) and NP 1.0 (magenta) data using single-channel features with or without footprint, combined across all six classes.

(G) Confusion matrices for all unit classification using 1-ch features + footprint.

(H) Confusion matrices for classification among the three types of optotagged interneurons only, using NEMO.

(legend continued on next page)

NP 1.0 probes, small-footprint waveforms were detected at a lower rate, but NS_S units still comprised about one-third of all NS units overall (Figure S17).

Classification of cortical inhibitory neurons

The dense and small recording sites of NP Ultra acquire greater-resolution information about the electrical features of recorded neurons, improving cell type classification from extracellular signatures. To test this, we took a decoding approach to assess classification performance. We first trained a logistic regression model between single optotagged types (PV, SST, or VIP) against untagged units, using all recorded waveform features (STAR Methods; see below) as predictors. This model performed well, especially compared with a model using waveform duration alone, both when using balanced sampling (89% correct for PV, 82% for SST, 83% for VIP; Figures 7A, 7B, andS18A) and sampling that maintained interneuron proportions approximately equal to those found in the cortex (Figures S18B–S18D). We extracted single-channel waveform features using the peak amplitude channel for each unit, which revealed waveform characteristics unique to each type of neuron discussed above (Figures 7C, 7D, and S19; STAR Methods, neuron features table). Reducing the dimensionality of the features revealed substantial, but incomplete, segregation of the cell classes according to these features (Figures 7E and S20). We therefore undertook a quantitative assessment of cell type classification.

Interneuron classification was improved by the dense sampling of NP Ultra compared with NP 1.0. To analyze this, we trained a non-linear supervised classifier (random forest) to predict the identity of each neuron among RS, NS_L, NS_S, PV, SST, and VIP types, with balanced groups (chance performance = 0.17; see STAR Methods). We assessed model performance when training on three different feature sets: single-channel waveform features (1-ch features; Figure 7C), the single-channel waveform itself, or all 1-ch features along with the footprint radius (1-ch wf, 1-ch + footprint; Figures 7D, 7F, and S20). Because classifier accuracy was not improved using the single-channel waveform over single-channel features using all units, we focus here only on analyses using the single-channel features and footprint. Overall, classification performance on both of these feature sets was significantly above chance for these six classes (mean ± SD accuracy: 1-ch feats. = 0.63 ± 0.03, 1-ch feats. + footprint = 0.67 ± 0.04). To compare NP Ultra waveforms with lower-resolution NP 1.0 waveforms, we spatially resampled data from NP Ultra-recorded units to provide a direct unit-for-unit comparison (Figures 2E and 7F; see STAR Methods). NP Ultra-recorded units had better performance than NP 1.0, regardless of the features used in classification (mean accuracy for NP 1.0-like: 1-ch feats. = 0.44 ± 0.16, 1-ch feats. + footprint = 0.46 ± 0.15, $p << 0.001$ for each comparison, independent t test, multiple comparisons corrected via Benjamini-Hochberg method). The improvement in performance of NP Ultra over NP 1.0-like data extended to classification using all six unit class categories as well: RS units were classified with the highest accuracy (mean ± SD = 0.83 ± 0.10) followed by NS_S (0.71 ± 0.08), SST (0.67 ± 0.10), PV (0.59 ± 0.09), VIP (0.49 ± 0.09), and NS_L (0.48 ± 0.11; Figures 7G and 7I). Note that errors between PV and NS_L, which represent the largest source of error (Figure 7G), presumably reflect the fact that these two classes are largely overlapping, as discussed above.

Classification performance was even higher when considering only the three unit classes for which we have ground-truth identification, and this was still superior for NP Ultra relative to 1.0. We performed classification using only those neurons that had been optotagged (PV, SST, and VIP; Figure 7H). To achieve maximum accuracy, we used the neuronal embeddings via multimodal contrastive learning (NEMO) algorithm[55] for classification, an approach based on contrastive learning from waveform and autocorrelogram features (see STAR Methods). The accuracy among only these three types was high, 80.33% on average (Figure 7H).

The importance of spatial footprint as a feature useful for discriminating unit class was reinforced by further analyses. Mean classification accuracy using NP Ultra data, but not NP 1.0-like data, increased significantly when including footprint as a feature relative to performance without footprint (Figure 7F; p = 0.0003). Classification of PV, SST, VIP, and NS_L improved when footprint was included and by a greater margin when compared with NP 1.0-like classification (Figure 7I). Next, we iteratively removed each feature and assessed the difference in overall performance, a measure of feature importance (Figure 7J). Doing so revealed that removing the footprint impacted classification performance as much as the spike duration and baseline firing rate but less than the average inter-spike interval (ISI). Classifier accuracy was still above chance levels, even when only decoding from footprint, average ISI, and baseline firing rate (FR) (Figure 7J, inset; mean accuracy = 0.38 ± 0.03). In summary, we demonstrate that NP Ultra probes offer an enhanced ability to discriminate unit classes recorded from the visual cortex compared with classifiers using NP 1.0-like data and that they do so in particular because of the high-resolution spatial information captured by NP Ultra.

DISCUSSION

Here, we introduce NP Ultra, a device capable of recording extracellular neural activity with an unprecedented site density (1.3 sites/μm). These new probes have small site size and spacing, resulting in a trade-off in recording span compared with NP 1.0 probes (288 μm vs. 3,840 μm vertical span) but allowing the detailed spatial structure of electrical fields to be sampled with unprecedented resolution. By harnessing this improved spatial resolution for recording extracellular data, we demonstrate significant improvements in extracellular data quality, including higher spike amplitudes and improved SNRs, resulting in increased yield of functionally responsive neurons. Recordings made with NP Ultra probes capture subcellular features—axonal and dendritic signals—and provide a new window into the biophysics of action

---

(I) Difference in true positive (TP) rate between NP Ultra and NP 1.0-like data.

(J) Classifier accuracy (mean ± 95% CI) across all unit classes when one feature is iteratively excluded. $^{*}p < 0.05$; $^{****}p < 0.001$ (t test with Benjamini-Hochberg correction). Dashed line, mean classifier accuracy with all 1-ch features + footprint. Inset, accuracy when no 1-ch features are included.

See also Figures S18–S20 and the neuron features table in the STAR Methods.

potential initiation and propagation. Finally, recordings at this density offer enhanced discrimination between cell types, specifically demonstrated for interneuron cell types within the visual cortex. These devices therefore enable high-resolution measurements across multiple brain regions and species. Moreover, our shared large-scale datasets provide a useful resource for spike-sorting algorithm development, for electrode array design, and for biophysical modeling.

The NP Ultra device may be optimal for multiple experimental objectives but has tradeoffs in recording span vs. density relative to other electrophysiological options. NP Ultra probes are particularly suitable, relative to NP 1.0 and 2.0, for maximizing yield from thin layers or small structures, such as individual cortical layers, the CA1 pyramidal layer, or subcortical nuclei including the claustrum and parts of thalamus, basal ganglia, midbrain, and hindbrain. NP Ultra will also be useful for studies of dendritic back-propagation, axonal signaling, and cell-type-specific coding when the required temporal resolution, brain region, or species is incompatible with imaging-based approaches.

A population of small-footprint waveforms was detected using NP Ultra probes across brain regions in different species, operationally defined here as units with an electrical waveform extent of less than 20 μm (smaller than the smallest distance between contacts on an NP 1.0 probe). In the mouse visual cortex, we observed that recordings from identified axons all exhibit small footprints. Despite the commonly accepted wisdom that axonal spikes have early positive peaks,[56–58] we observed a fraction of axonal waveforms lacking such positive peaks, consistent with simulations of recordings from nodes of Ranvier in myelinated axons.[23] The distributions of small-footprint waveforms within the cortex likely differ across cortical layers due to an increased density of axonal myelination toward deeper layers.[59] Moreover, although recordings of axonal spikes have been reported with Neuropixels probes[60,61] and with other devices,[62–66] it has been assumed that this is only possible in limited situations when axons have particularly favorable properties.[49,67] Here, we demonstrate these putative axonal recordings in all 15 brain regions and 4 species that we tested, establishing that NP Ultra probes can reliably achieve these recordings. Careful confirmation of the identity of these units will be required in each brain area in the future.

In the mouse DG and fish CB, we observed a significant fraction of small-footprint waveforms that might represent action potentials from small neuron types, axons, or both. Both the DG and CB are notable for their populations of granule cells with very small somata. Considering DG granule cells, however, previous studies have indicated that they are relatively quiescent[32,68,69] and not typically NS,[70] unlike the DG waveforms we recorded. It is also possible that the small-footprint waveforms in the DG are hilar interneurons.[71] Therefore, although it appears plausible that a subset of the units in our recordings may represent extracellular measurements of granule cells or interneurons in the DG and CB, this cannot be decisively assessed without further ground-truth experiments, such as recording genetically identified granule cells via optotagging.

In the visual cortex, the narrow action potential waveform ($\leq$0.4 ms) spikes have traditionally been associated with putatively PV-expressing NS inhibitory interneurons[26,27,72] because only a minority of SST[72], VIP,[73] and excitatory neurons[74,75] have NS waveforms. We discovered that the majority of optotagged neurons from genetically identified inhibitory subclasses exhibited large waveform footprints, consistent with their soma sizes being comparable with those of pyramidal neurons.[76,77] Our results indicate that PV+ optotagged neurons correspond to large-footprint NS units (NS_L), while NS_S units represent axon segments of both excitatory and inhibitory neurons. NS_S units constitute a small, yet significant, portion of the total units ($\sim$10%) and almost one-third of all NS units in NP 1.0 data. Reliable identification of putative PV+ interneurons therefore requires considering both waveform duration and footprint, without which approximately one-third of those units identified by waveform duration alone may be misidentified.

Our ability to classify cell types of recorded neurons was generally high within each cell type, and classification between cell types was significantly improved using NP Ultra compared with 1.0 probes. Nevertheless, our findings are applicable to existing recordings made with previous probes, enabling the identification of recorded units as PV+, VIP+, SST+, or other based on single-channel waveforms with a reasonable level of accuracy. In fact, our category of "untagged" units includes neurons from the PV, VIP, and SST cell types, which likely lead to an underestimation of classification accuracy (i.e., some untagged units labeled by the classifier as VIP might in fact be VIP+, though this is counted as an error). In the future, unit classification using a variety of additional metrics, such as non-linear waveform features,[34] autocorrelograms,[27,30,32] and oscillatory phase locking,[78] as well as alternative machine learning approaches,[35,36,79–81] may yield even greater performance.

Taken together, our findings collectively highlight the advantages of electrophysiological probes with increased site density for a wide range of neuroscience applications, including maximizing yield in targeted regions, sensitively detecting small-footprint waveforms, and discriminating cell types.

RESOURCE AVAILABILITY

Lead contact

Requests for further information and resources should be directed to, and will be fulfilled by, the lead contact, Nicholas A. Steinmetz (nick.steinmetz@gmail.com).

Materials availability

As of the time of writing, NP Ultra probes were available for purchase at https://www.neuropixels.org/specialty-products under the name "Neuropixels 1.0 HD" (for "high density"). Future availability is subject to supply constraints.

Data and code availability

- Spatiotemporal waveforms of 4,666 single units recorded in awake mice, along with spike times, are available at https://doi.org/10.6084/m9.figshare.19493588, and waveform movies are browsable at https://npultra.steinmetzlab.net/. NP Ultra dataset for imposed motion with visual responses pre- and post-motion in the visual cortex is available at https://dandiarchive.org/dandiset/000957.
- Code for computing spatial footprints of recorded neurons, in Python and in MATLAB, is provided at https://github.com/zhiwen10/Neuropixels-footprint and is publicly available at https://doi.org/10.5281/zenodo.16929837. DARTsort code is available at https://github.com/cwindolf/dartsort/tree/uhd_np and is publicly available at https://doi.org/10.5281/zenodo.16943075.
- Any additional information required to reanalyze the data reported in this work is available from the lead contact upon request.

ACKNOWLEDGMENTS

We thank NIH program officers Ned Talley, Sahana Kukke, Michele Pucak, and Grace Hwang for their support, and we thank Tim Gardner and Cindy Chestek for their advice and guidance. We thank Bill Karsh for SpikeGLX software modifications, enabling the use of NP Ultra probes. This research program was funded by the NIH BRAIN Initiative (U01NS113252 to N.A.S., S.R.O., and T.D.H.). Additional support was provided by the Pew Biomedical Scholars Program (N.A.S.), the Klingenstein-Simons Fellowship in Neuroscience (N.A.S.), the Max Planck Society (G.L.), the European Research Council under the European Union's Horizon 2020 Research and Innovation Programme (grant agreement no. 834446 to G.L. and AdG 695709 to M.H.), the NIH (R01 NS118448 and R01 NS075023 to N.B.S.; F30 EY035113 to J.R.S.; R01 EY029601 and U01 NS131810 to A.P. and W.B.; U19 NS107613 to L.P.; and U19 NS123716 to L.P. and N.A.S.), the Wellcome Trust (PRF 201225 and 224688 to M.H., SHWF 221674 to L.F.R., and collaborative award 204915 to M.C., M.H., and T.D.H.), the Gatsby Charitable Foundation (GAT3708 to L.P.), the Giovanni Armenise Harvard Foundation (CDA to L.F.R.), the Human Technopole (HT-ECF 3588 to L.F.R.), the NSF and DoD OUSD (R&E) under Cooperative Agreement PHY-2229929 (The NSF AI Institute for Artificial and Natural Intelligence, to L.P.), the Simons Foundation (to L.P.), and the NSF (IOS 2115007 to N.B.S.). G.M. is supported by a Boehringer Ingelheim Fonds PhD Fellowship. The primate research procedures were supported by the NIH P51 (OD010425) to the WaNPRC, and animal breeding was supported by NIH U42 (OD011123). Computational modeling work was supported by the European Union Horizon 2020 Research and Innovation Programme under grant agreement no. 945539 Human Brain Project SGA3 and no. 101147319 EBRAINS 2.0 (G.T.E. and T.V.N.). Additional funding for this project was provided by the Allen Institute. We thank the Allen Institute founder, Paul G. Allen, for his vision, encouragement, and support. We thank the Transgenic Colony management, Animal Care, and Laboratory Animal Services teams at the Allen Institute for caring for mice in this study.

AUTHOR CONTRIBUTIONS

Z.Y. collected brain-wide acute mouse recordings and pharmacology experiments. A.M.S. and S.M. collected data with optotagging. Z.Y. and J.R.S. collected data with imposed probe motion and visual stimuli. J.C. performed noise and gain measurements. A.M.S. performed light sensitivity measurements. S.C. collected acute mouse recordings. J.H.S. wrote software for data acquisition. T.N. and W.B. collected non-human primate recordings. F.P. and N.B.S. collected recordings from electric fish. S.W. collected recordings from bearded dragon lizards. L.F.R. and G.M. collected and analyzed data on dendritic back-propagation. J.B., C.W., C.H., and L.P. developed the spike-sorting methods. H.Y. and C.H. performed cell classification analyses with NEMO. Z.Y., A.M.S., J.C., J.B., J.R.S., and N.A.S. analyzed data. D.B. developed the data exploration website. C.M.L., B.C.R., and B.D. performed engineering and fabrication of NP Ultra probes. T.V.N. wrote the computational model and N.A.S. analyzed the output. Z.Y., A.M.S., J.C., J.B., J.R.S., L.P., S.R.O., and N.A.S. wrote the original draft manuscript. All authors reviewed and edited the manuscript. S.R.O., T.D.H., and N.A.S. obtained primary funding. X.J., M.C., M.H., L.F.R., G.T.E., G.L., N.B.S., W.B., A.P., C.M.L., B.D., L.P., J.H.S., C.K., S.R.O., T.D.H., and N.A.S. supervised aspects of the work.

DECLARATION OF INTERESTS

C.K. holds an executive position and has a financial interest in Intrinsic Powers, Inc., a company whose purpose is to develop a device that can be used in the clinic to assess the presence and absence of consciousness in patients. This does not pose any conflict of interest with regard to the work undertaken for this publication. B.R., C.M.L., and B.D. are employees of IMEC vzw, a nonprofit research institute that manufactures, sells, and distributes the Neuropixels probes, at cost, to the research community. IMEC vzw holds patents US10811542B2, US10044325B2, and US9384990B2 related to the NP 1.0 technology that is built upon in this work. M.C., M.H., and L.P. are members of *Neuron*'s advisory board.

STAR★METHODS

Detailed methods are provided in the online version of this paper and include the following:

- KEY RESOURCES TABLE
- EXPERIMENTAL MODEL AND STUDY PARTICIPANT DETAILS
- METHOD DETAILS
  - Probe noise model
  - Noise and gain characterization
  - Crosstalk estimation
  - Light artifact tests
  - Recordings from diverse brain regions in the mouse
  - Muscimol experiments
  - Spike sorting methods
  - Methods for site pattern comparison using spatial resampling
  - Analyses of sorting quality
  - Yield, decoding, and stability testing with imposed probe-brain motion
  - Biophysical simulations
  - Recordings from species other than mouse
  - Brain region abbreviations
  - Optotagging
  - Supervised waveform classification of inhibitory neurons
  - Multimodal classification of inhibitory neurons

SUPPLEMENTAL INFORMATION

Supplemental information can be found online at https://doi.org/10.1016/j.neuron.2025.08.030.

Received: April 6, 2024
Revised: April 14, 2025
Accepted: August 29, 2025
Published: September 30, 2025

REFERENCES

1. Jun, J.J., Steinmetz, N.A., Siegle, J.H., Denman, D.J., Bauza, M., Barbarits, B., Lee, A.K., Anastassiou, C.A., Andrei, A., Aydın, Ç., et al. (2017). Fully integrated silicon probes for high-density recording of neural activity. Nature *551*, 232–236. https://doi.org/10.1038/nature24636.
2. Steinmetz, N.A., Koch, C., Harris, K.D., and Carandini, M. (2018). Challenges and opportunities for large-scale electrophysiology with Neuropixels probes. Curr. Opin. Neurobiol. *50*, 92–100. https://doi.org/10.1016/j.conb.2018.01.009.
3. Steinmetz, N.A., Aydin, C., Lebedeva, A., Okun, M., Pachitariu, M., Bauza, M., Beau, M., Bhagat, J., Böhm, C., Broux, M., et al. (2021). Neuropixels 2.0: A miniaturized high-density probe for stable, long-term brain recordings. Science *372*, eabf4588. https://doi.org/10.1126/science.abf4588.
4. Steinmetz, N.A., Zatka-Haas, P., Carandini, M., and Harris, K.D. (2019). Distributed coding of choice, action and engagement across the mouse brain. Nature *576*, 266–273. https://doi.org/10.1038/s41586-019-1787-x.
5. Norimoto, H., Fenk, L.A., Li, H.-H., Tosches, M.A., Gallego-Flores, T., Hain, D., Reiter, S., Kobayashi, R., Macias, A., Arends, A., et al. (2020). A claustrum in reptiles and its role in slow-wave sleep. Nature *578*, 413–418. https://doi.org/10.1038/s41586-020-1993-6.
6. Metzen, M.G., and Chacron, M.J. (2021). Population Coding of Natural Electrosensory Stimuli by Midbrain Neurons. J. Neurosci. *41*, 3822–3841. https://doi.org/10.1523/JNEUROSCI.2232-20.2021.
7. Siegle, J.H., Jia, X., Durand, S., Gale, S., Bennett, C., Graddis, N., Heller, G., Ramirez, T.K., Choi, H., Luviano, J.A., et al. (2021). Survey of spiking

in the mouse visual system reveals functional hierarchy. Nature *592*, 86–92. https://doi.org/10.1038/s41586-020-03171-x.

8. Chung, J.E., Sellers, K.K., Leonard, M.K., Gwilliams, L., Xu, D., Dougherty, M.E., Kharazia, V., Metzger, S.L., Welkenhuysen, M., Dutta, B., et al. (2022). High-density single-unit human cortical recordings using the Neuropixels probe. Neuron *110*, 2409–2421.e3. https://doi.org/10.1016/j.neuron.2022.05.007.
9. Paulk, A.C., Kfir, Y., Khanna, A.R., Mustroph, M.L., Trautmann, E.M., Soper, D.J., Stavisky, S.D., Welkenhuysen, M., Dutta, B., Shenoy, K.V., et al. (2022). Large-scale neural recordings with single neuron resolution using Neuropixels probes in human cortex. Nat. Neurosci. *25*, 252–263. https://doi.org/10.1038/s41593-021-00997-0.
10. Trautmann, E.M., Hesse, J.K., Stine, G.M., Xia, R., Zhu, S., O'Shea, D.J., Karsh, B., Colonell, J., Lanfranchi, F.F., Vyas, S., et al. (2025). Large-scale high-density brain-wide neural recording in nonhuman primates. Nat. Neurosci. *28*, 1562–1575. https://doi.org/10.1038/s41593-025-01976-5.
11. Allen, W.E., Chen, M.Z., Pichamoorthy, N., Tien, R.H., Pachitariu, M., Luo, L., and Deisseroth, K. (2019). Thirst regulates motivated behavior through modulation of brainwide neural population dynamics. Science *364*, 253. https://doi.org/10.1126/science.aav3932.
12. Musall, S., Kaufman, M.T., Juavinett, A.L., Gluf, S., and Churchland, A.K. (2019). Single-trial neural dynamics are dominated by richly varied movements. Nat. Neurosci. *22*, 1677–1686. https://doi.org/10.1038/s41593-019-0502-4.
13. Stringer, C., Pachitariu, M., Steinmetz, N., Reddy, C.B., Carandini, M., and Harris, K.D. (2019). Spontaneous behaviors drive multidimensional, brainwide activity. Science *364*, 255. https://doi.org/10.1126/science.aav7893.
14. Vesuna, S., Kauvar, I.V., Richman, E., Gore, F., Oskotsky, T., Sava-Segal, C., Luo, L., Malenka, R.C., Henderson, J.M., Nuyujukian, P., et al. (2020). Deep posteromedial cortical rhythm in dissociation. Nature *586*, 87–94. https://doi.org/10.1038/s41586-020-2731-9.
15. Gardner, R.J., Hermansen, E., Pachitariu, M., Burak, Y., Baas, N.A., Dunn, B.A., Moser, M.-B., and Moser, E.I. (2022). Toroidal topology of population activity in grid cells. Nature *602*, 123–128. https://doi.org/10.1038/s41586-021-04268-7.
16. Jia, X., Siegle, J.H., Durand, S., Heller, G., Ramirez, T.K., Koch, C., and Olsen, S.R. (2022). Multi-regional module-based signal transmission in mouse visual cortex. Neuron *110*, 1585–1598.e9. https://doi.org/10.1016/j.neuron.2022.01.027.
17. Chen, S., Liu, Y., Wang, Z.A., Colonell, J., Liu, L.D., Hou, H., Tien, N.-W., Wang, T., Harris, T., Druckmann, S., et al. (2024). Brain-wide neural activity underlying memory-guided movement. Cell *187*, 676–691.e16. https://doi.org/10.1016/j.cell.2023.12.035.
18. International; Brain Laboratory, Benson, B., Benson, J., Birman, D., Bonacchi, N., Carandini, M., Catarino, J.A., Chapuis, G.A., Churchland, A.K., and Dan, Y. (2023). A Brain-Wide Map of Neural Activity during Complex Behaviour. Preprint at bioRxiv. https://doi.org/10.1101/2023.07.04.547681.
19. Buzsaki, G. (2006). Rhythms of the Brain (Oxford University Press).
20. Nunez, P.L., and Srinivasan, R. (2006). Electric Fields of the Brain: the Neurophysics of EEG (Oxford University Press).
21. Katzner, S., Nauhaus, I., Benucci, A., Bonin, V., Ringach, D.L., and Carandini, M. (2009). Local Origin of Field Potentials in Visual Cortex. Neuron *61*, 35–41. https://doi.org/10.1016/j.neuron.2008.11.016.
22. Buzsáki, G., Anastassiou, C.A., and Koch, C. (2012). The origin of extracellular fields and currents—EEG, ECoG, LFP and spikes. Nat. Rev. Neurosci. *13*, 407–420. https://doi.org/10.1038/nrn3241.
23. Halnes, G., Ness, T.V., Næss, S., Hagen, E., Pettersen, K.H., and Einevoll, G.T. (2024). Electric Brain Signals (Cambridge University Press). https://doi.org/10.1017/9781009039826.
24. Gouwens, N.W., Sorensen, S.A., Baftizadeh, F., Budzillo, A., Lee, B.R., Jarsky, T., Alfiler, L., Baker, K., Barkan, E., Berry, K., et al. (2020). Integrated Morphoelectric and Transcriptomic Classification of Cortical GABAergic Cells. Cell *183*, 935–953.e19. https://doi.org/10.1016/j.cell.2020.09.057.
25. Yao, Z., Van Velthoven, C.T.J., Nguyen, T.N., Goldy, J., Sedeno-Cortes, A.E., Baftizadeh, F., Bertagnolli, D., Casper, T., Chiang, M., Crichton, K., et al. (2021). A taxonomy of transcriptomic cell types across the isocortex and hippocampal formation. Cell *184*, 3222–3241.e26. https://doi.org/10.1016/j.cell.2021.04.021.
26. McCormick, D.A., Connors, B.W., Lighthall, J.W., and Prince, D.A. (1985). Comparative electrophysiology of pyramidal and sparsely spiny stellate neurons of the neocortex. J. Neurophysiol. *54*, 782–806. https://doi.org/10.1152/jn.1985.54.4.782.
27. Barthó, P., Hirase, H., Monconduit, L., Zugaro, M., Harris, K.D., and Buzsáki, G. (2004). Characterization of neocortical principal cells and interneurons by network interactions and extracellular features. J. Neurophysiol. *92*, 600–608. https://doi.org/10.1152/jn.01170.2003.
28. Mitchell, J.F., Sundberg, K.A., and Reynolds, J.H. (2007). Differential Attention-Dependent Response Modulation across Cell Classes in Macaque Visual Area V4. Neuron *55*, 131–141. https://doi.org/10.1016/j.neuron.2007.06.018.
29. Niell, C.M., and Stryker, M.P. (2008). Highly Selective Receptive Fields in Mouse Visual Cortex. J. Neurosci. *28*, 7520–7536. https://doi.org/10.1523/JNEUROSCI.0623-08.2008.
30. Yamin, H.G., Stern, E.A., and Cohen, D. (2013). Parallel Processing of Environmental Recognition and Locomotion in the Mouse Striatum. J. Neurosci. *33*, 473–484. https://doi.org/10.1523/JNEUROSCI.4474-12.2013.
31. Roux, L., Stark, E., Sjulson, L., and Buzsáki, G. (2014). In vivo optogenetic identification and manipulation of GABAergic interneuron subtypes. Curr. Opin. Neurobiol. *26*, 88–95. https://doi.org/10.1016/j.conb.2013.12.013.
32. Senzai, Y., and Buzsáki, G. (2017). Physiological Properties and Behavioral Correlates of Hippocampal Granule Cells and Mossy Cells. Neuron *93*, 691–704.e5. https://doi.org/10.1016/j.neuron.2016.12.011.
33. Yu, J., Hu, H., Agmon, A., and Svoboda, K. (2019). Recruitment of GABAergic Interneurons in the Barrel Cortex during Active Tactile Behavior. Neuron *104*, 412–427.e4. https://doi.org/10.1016/j.neuron.2019.07.027.
34. Lee, E.K., Balasubramanian, H., Tsolias, A., Anakwe, S.U., Medalla, M., Shenoy, K.V., and Chandrasekaran, C. (2021). Non-linear dimensionality reduction on extracellular waveforms reveals cell type diversity in premotor cortex. eLife *10*, e67490. https://doi.org/10.7554/eLife.67490.
35. Lee, E.K., Gül, A.E., Heller, G., Lakunina, A., Jaramillo, S., Przytycki, P.F., and Chandrasekaran, C. (2024). PhysMAP - interpretable *in vivo* neuronal cell type identification using multi-modal analysis of electrophysiological data. Preprint at bioRxiv. https://doi.org/10.1101/2024.02.28.582461.
36. Beau, M., Herzfeld, D.J., Naveros, F., Hemelt, M.E., D'Agostino, F., Oostland, M., Sánchez-López, A., Chung, Y.Y., Maibach, M., Kyranakis, S., et al. (2025). A deep learning strategy to identify cell types across species from high-density extracellular recordings. Cell *188*, 2218–2234.e22. https://doi.org/10.1016/j.cell.2025.01.041.
37. Buccino, A.P., Kordovan, M., Ness, T.V., Merkt, B., Häfliger, P.D., Fyhn, M., Cauwenberghs, G., Rotter, S., and Einevoll, G.T. (2018). Combining biophysical modeling and deep learning for multielectrode array neuron localization and classification. J. Neurophysiol. *120*, 1212–1232. https://doi.org/10.1152/jn.00210.2018.
38. Jia, X., Siegle, J.H., Bennett, C., Gale, S.D., Denman, D.J., Koch, C., and Olsen, S.R. (2019). High-density extracellular probes reveal dendritic backpropagation and facilitate neuron classification. J. Neurophysiol. *121*, 1831–1847. https://doi.org/10.1152/jn.00680.2018.
39. López, C.M., Welkenhuysen, M., Musa, S., Eberle, W., Bartic, C., Puers, R., and Gielen, G. (2012). Towards a noise prediction model for in vivo

neural recording. In 2012 Annual International Conference of the IEEE Engineering in Medicine and Biology Society (IEEE), pp. 759–762. https://doi.org/10.1109/EMBC.2012.6346042.

40. Rey, H.G., Pedreira, C., and Quian Quiroga, R. (2015). Past, present and future of spike sorting techniques. Brain Res. Bull. *119*, 106–117. https://doi.org/10.1016/j.brainresbull.2015.04.007.
41. Boussard, J., Windolf, C., Hurwitz, C., Lee, H.D., Yu, H., Winter, O., and Paninski, L. (2023). DARTsort: A modular drift tracking spike sorter for high-density multi-electrode probes. Preprint at bioRxiv. https://doi.org/10.1101/2023.08.11.553023.
42. Boussard, J., Varol, E., Lee, H.D., Dethe, N., and Paninski, L. (2021). Three-dimensional spike localization and improved motion correction for Neuropixels recordings. Preprint at bioRxiv. https://doi.org/10.1101/2021.11.05.467503.
43. Windolf, C., Yu, H., Paulk, A.C., Meszéna, D., Muñoz, W., Boussard, J., Hardstone, R., Caprara, I., Jamali, M., Kfir, Y., et al. (2025). DREDge: robust motion correction for high-density extracellular recordings across species. Nat. Methods *22*, 788–800. https://doi.org/10.1038/s41592-025-02614-5.
44. Banga, K., Benson, J., Bhagat, J., Biderman, D., Birman, D., Bonacchi, N., Bruijns, S.A., Campbell, R.A., Carandini, M., et al.; International Brain Laboratory (2025). Reproducibility of in vivo electrophysiological measurements in mice. eLife *13*, RP100840. https://doi.org/10.7554/eLife.100840.3.
45. Canakci, S., Toy, M.F., Inci, A.F., Liu, X., and Kuzum, D. (2017). Computational analysis of network activity and spatial reach of sharp wave-ripples. PLoS One *12*, e0184542. https://doi.org/10.1371/journal.pone.0184542.
46. Viswam, V., Obien, M., Frey, U., Franke, F., and Hierlemann, A. (2017). Acquisition of bioelectrical signals with small electrodes. In 2017 IEEE Biomedical Circuits and Systems Conference (BioCAS) (IEEE), pp. 1–4.
47. Hill, M., Rios, E., Sudhakar, S.K., Roossien, D.H., Caldwell, C., Cai, D., Ahmed, O.J., Lempka, S.F., and Chestek, C.A. (2018). Quantitative simulation of extracellular single unit recording from the surface of cortex. J. Neural Eng. *15*, 056007. https://doi.org/10.1088/1741-2552/aacdb8.
48. Fiáth, R., Raducanu, B.C., Musa, S., Andrei, A., Lopez, C.M., Welkenhuysen, M., Ruther, P., Aarts, A., and Ulbert, I. (2019). Fine-scale mapping of cortical laminar activity during sleep slow oscillations using high-density linear silicon probes. J. Neurosci. Methods *316*, 58–70. https://doi.org/10.1016/j.jneumeth.2018.08.020.
49. McColgan, T., Liu, J., Kuokkanen, P.T., Carr, C.E., Wagner, H., and Kempter, R. (2017). Dipolar extracellular potentials generated by axonal projections. eLife *6*, e26106. https://doi.org/10.7554/eLife.26106.
50. Buzsáki, G., and Kandel, A. (1998). Somadendritic Backpropagation of Action Potentials in Cortical Pyramidal Cells of the Awake Rat. J. Neurophysiol. *79*, 1587–1591. https://doi.org/10.1152/jn.1998.79.3.1587.
51. Gold, C., Henze, D.A., Koch, C., and Buzsáki, G. (2006). On the origin of the extracellular action potential waveform: A modeling study. J. Neurophysiol. *95*, 3113–3128. https://doi.org/10.1152/jn.00979.2005.
52. Stuart, G., Schiller, J., and Sakmann, B. (1997). Action potential initiation and propagation in rat neocortical pyramidal neurons. J. Physiol. *505*, 617–632. https://doi.org/10.1111/j.1469-7793.1997.617ba.x.
53. Gilman, J.P., Medalla, M., and Luebke, J.I. (2017). Area-Specific Features of Pyramidal Neurons—a Comparative Study in Mouse and Rhesus Monkey. Cereb. Cortex *27*, 2078–2094. https://doi.org/10.1093/cercor/bhw062.
54. Lima, S.Q., Hromádka, T., Znamenskiy, P., and Zador, A.M. (2009). PINP: A New Method of Tagging Neuronal Populations for Identification during In Vivo Electrophysiological Recording. PLoS One *4*, e6099. https://doi.org/10.1371/journal.pone.0006099.
55. Yu, H., Lyu, H., Xu, E.Y., Windolf, C., Lee, E.K., Yang, F., Shelton, A.M., Olsen, S., Minavi, S., Winter, O., et al. (2025). In vivo cell-type and brain region classification via multimodal contrastive learning. Preprint at bioRxiv. https://doi.org/10.1101/2024.11.05.622159.
56. Cooper, G.F., Robson, J.G., and Waldron, I. (1969). The action potentials recorded from undamaged nerve fibres with micro-electrodes. J. Physiol. *200*, 9P–11P.
57. Deligkaris, K., Bullmann, T., and Frey, U. (2016). Extracellularly Recorded Somatic and Neuritic Signal Shapes and Classification Algorithms for High-Density Microelectrode Array Electrophysiology. Front. Neurosci. *10*, 421. https://doi.org/10.3389/fnins.2016.00421.
58. Someck, S., Levi, A., Sloin, H.E., Spivak, L., Gattegno, R., and Stark, E. (2023). Positive and biphasic extracellular waveforms correspond to return currents and axonal spikes. Commun. Biol. *6*, 950. https://doi.org/10.1038/s42003-023-05328-6.
59. Tomassy, G.S., Berger, D.R., Chen, H.-H., Kasthuri, N., Hayworth, K.J., Vercelli, A., Seung, H.S., Lichtman, J.W., and Arlotta, P. (2014). Distinct Profiles of Myelin Distribution Along Single Axons of Pyramidal Neurons in the Neocortex. Science *344*, 319–324. https://doi.org/10.1126/science.1249766.
60. Schröder, S., Steinmetz, N.A., Krumin, M., Pachitariu, M., Rizzi, M., Lagnado, L., Harris, K.D., and Carandini, M. (2020). Arousal Modulates Retinal Output. Neuron *107*, 487–495.e9. https://doi.org/10.1016/j.neuron.2020.04.026.
61. Sibille, J., Gehr, C., Benichov, J.I., Balasubramanian, H., Teh, K.L., Lupashina, T., Vallentin, D., and Kremkow, J. (2022). High-density electrode recordings reveal strong and specific connections between retinal ganglion cells and midbrain neurons. Nat. Commun. *13*, 5218. https://doi.org/10.1038/s41467-022-32775-2.
62. Merrill, E.G., Wall, P.D., and Yaksh, T.L. (1978). Properties of two unmyelinated fibre tracts of the central nervous system: lateral Lissauer tract, and parallel fibres of the cerebellum. J. Physiol. *284*, 127–145. https://doi.org/10.1113/jphysiol.1978.sp012531.
63. Goldberg, J.H., and Fee, M.S. (2012). A cortical motor nucleus drives the basal ganglia-recipient thalamus in singing birds. Nat. Neurosci. *15*, 620–627. https://doi.org/10.1038/nn.3047.
64. Robbins, A.A., Fox, S.E., Holmes, G.L., Scott, R.C., and Barry, J.M. (2013). Short duration waveforms recorded extracellularly from freely moving rats are representative of axonal activity. Front. Neural Circuits *7*, 181. https://doi.org/10.3389/fncir.2013.00181.
65. Barthó, P., Slézia, A., Mátyás, F., Faradzs-Zade, L., Ulbert, I., Harris, K. D., and Acsády, L. (2014). Ongoing Network State Controls the Length of Sleep Spindles via Inhibitory Activity. Neuron *82*, 1367–1379. https://doi.org/10.1016/j.neuron.2014.04.046.
66. Sun, S.H., Almasi, A., Yunzab, M., Zehra, S., Hicks, D.G., Kameneva, T., Ibbotson, M.R., and Meffin, H. (2021). Analysis of extracellular spike waveforms and associated receptive fields of neurons in cat primary visual cortex. J. Physiol. *599*, 2211–2238. https://doi.org/10.1113/JP280844.
67. Barthó, P. (2021). Extracellular recording of axonal spikes in the visual cortex. J. Physiol. *599*, 2131. https://doi.org/10.1113/JP281404.
68. Neubrandt, M., Oláh, V.J., Brunner, J., Marosi, E.L., Soltesz, I., and Szabadics, J. (2018). Single Bursts of Individual Granule Cells Functionally Rearrange Feedforward Inhibition. J. Neurosci. *38*, 1711–1724. https://doi.org/10.1523/JNEUROSCI.1595-17.2018.
69. McHugh, S.B., Lopes-dos-Santos, V., Gava, G.P., Hartwich, K., Tam, S. K.E., Bannerman, D.M., and Dupret, D. (2022). Adult-born dentate granule cells promote hippocampal population sparsity. Nat. Neurosci. *25*, 1481–1491. https://doi.org/10.1038/s41593-022-01176-5.
70. Pedroni, A., Minh, D.D., Mallamaci, A., and Cherubini, E. (2014). Electrophysiological characterization of granule cells in the dentate gyrus immediately after birth. Front. Cell. Neurosci. *8*, 44. https://doi.org/10.3389/fncel.2014.00044.
71. Yuan, M., Meyer, T., Benkowitz, C., Savanthrapadian, S., Ansel-Bollepalli, L., Foggetti, A., Wulff, P., Alcami, P., Elgueta, C., and Bartos, M. (2017). Somatostatin-positive interneurons in the dentate gyrus of

mice provide local- and long-range septal synaptic inhibition. eLife *6*, e21105. https://doi.org/10.7554/eLife.21105.

72. Kvitsiani, D., Ranade, S., Hangya, B., Taniguchi, H., Huang, J.Z., and Kepecs, A. (2013). Distinct behavioural and network correlates of two interneuron types in prefrontal cortex. Nature *498*, 363–366. https://doi.org/10.1038/nature12176.
73. Petersen, P.C., Siegle, J.H., Steinmetz, N.A., Mahallati, S., and Buzsáki, G. (2021). CellExplorer: A framework for visualizing and characterizing single neurons. Neuron *109*, 3594–3608.e2. https://doi.org/10.1016/j.neuron.2021.09.002.
74. Nowak, L.G., Azouz, R., Sanchez-Vives, M.V., Gray, C.M., and McCormick, D.A. (2003). Electrophysiological Classes of Cat Primary Visual Cortical Neurons In Vivo as Revealed by Quantitative Analyses. J. Neurophysiol. *89*, 1541–1566. https://doi.org/10.1152/jn.00580.2002.
75. Lemon, R.N., Baker, S.N., and Kraskov, A. (2021). Classification of Cortical Neurons by Spike Shape and the Identification of Pyramidal Neurons. Cereb. Cortex *31*, 5131–5138. https://doi.org/10.1093/cercor/bhab147.
76. Beebe, N.L., Young, J.W., Mellott, J.G., and Schofield, B.R. (2016). Extracellular Molecular Markers and Soma Size of Inhibitory Neurons: Evidence for Four Subtypes of GABAergic Cells in the Inferior Colliculus. J. Neurosci. *36*, 3988–3999. https://doi.org/10.1523/JNEUROSCI.0217-16.2016.
77. Elabbady, L., Seshamani, S., Mu, S., Mahalingam, G., Schneider-Mizell, C., Bodor, A.L., Bae, J.A., Brittain, D., Buchanan, J., Bumbarger, D.J., et al. (2024). Perisomatic features enable efficient and dataset wide cell-type classifications Across large-scale electron microscopy volumes. Preprint at bioRxiv. https://doi.org/10.1101/2022.07.20.499976.
78. Reifenstein, E.T., Ebbesen, C.L., Tang, Q., Brecht, M., Schreiber, S., and Kempter, R. (2016). Cell-Type Specific Phase Precession in Layer II of the Medial Entorhinal Cortex. J. Neurosci. *36*, 2283–2288. https://doi.org/10.1523/JNEUROSCI.2986-15.2016.
79. Crawford, E., and Pineau, J. (2019). Spatially Invariant Unsupervised Object Detection with Convolutional Neural Networks. In AAAI Technical Track: Machine Learning, *33*, pp. 3412–3420. https://doi.org/10.1609/aaai.v33i01.33013412.
80. Tymochko, S., Munch, E., Dunion, J., Corbosiero, K., and Torn, R. (2020). Using persistent homology to quantify a diurnal cycle in hurricanes. Pattern Recognit. Lett. *133*, 137–143. https://doi.org/10.1016/j.patrec.2020.02.022.
81. Kingma, D.P., and Welling, M. (2022). Auto-encoding variational Bayes. Preprint at arXiv. https://doi.org/10.48550/arXiv.1312.6114.
82. Pachitariu, M., Steinmetz, N., Kadir, S., Carandini, M.D., and H.K.. (2016). Kilosort: realtime spike-sorting for extracellular electrophysiology with hundreds of channels. Preprint at bioRxiv. https://doi.org/10.1101/061481.
83. Yang, Z., Zhao, Q., Keefer, E., and Liu, W. (2009). Noise characterization, modeling, and reduction for in vivo neural recording. In Advances in Neural Information Processing Systems 22 (NIPS 2009).
84. Chen, S., and Svoboda, K. (2020). "Uniclear" Water-Based Brain Clearing for Light Sheet Imaging of Electrode Tracks. https://doi.org/10.17504/protocols.io.zndf5a6.
85. Lee, J., Mitelut, C., Shokri, H., Kinsella, I., Dethe, N., Wu, S., Li, K., Reyes, E.B., Turcu, D., Batty, E., et al. (2020). YASS: Yet Another Spike Sorter applied to large-scale multi-electrode array recordings in primate retina. Preprint at bioRxiv. https://doi.org/10.1101/2020.03.18.997924.
86. Hilgen, G., Sorbaro, M., Pirmoradian, S., Muthmann, J.-O., Kepiro, I.E., Ullo, S., Ramirez, C.J., Puente Encinas, A.P., Maccione, A., Berdondini, L., et al. (2017). Unsupervised spike sorting for large-scale, high-density multielectrode arrays. Cell Rep. *18*, 2521–2532. https://doi.org/10.1016/j.celrep.2017.02.038.
87. Malzer, C., and Baum, M. (2019). A Hybrid Approach to Hierarchical Density-Based Cluster Selection. Preprint at arXiv. https://doi.org/10.48550/ARXIV.1911.02282.
88. Swindale, N.V., and Spacek, M.A. (2014). Spike sorting for polytrodes: a divide and conquer approach. Front. Syst. Neurosci. *8*, 6. https://doi.org/10.3389/fnsys.2014.00006.
89. Robinson, D.A. (1968). The electrical properties of metal microelectrodes. Proc. IEEE *56*, 1065–1071. https://doi.org/10.1109/PROC.1968.6458.
90. Nelson, M.J., and Pouget, P. (2010). Do Electrode Properties Create a Problem in Interpreting Local Field Potential Recordings? J. Neurophysiol. *103*, 2315–2317. https://doi.org/10.1152/jn.00157.2010.
91. Hagen, E., Næss, S., Ness, T.V., and Einevoll, G.T. (2018). Multimodal Modeling of Neural Network Activity: Computing LFP, ECoG, EEG, and MEG Signals With LFPy 2.0. Front. Neuroinform. *12*, 92. https://doi.org/10.3389/fninf.2018.00092.
92. Carnevale, N.T., and Hines, M.L. (2006). The NEURON Book (Cambridge University Press). https://doi.org/10.1017/CBO9780511541612.
93. Hay, E., Hill, S., Schürmann, F., Markram, H., and Segev, I. (2011). Models of Neocortical Layer 5b Pyramidal Cells Capturing a Wide Range of Dendritic and Perisomatic Active Properties. PLoS Comput. Biol. *7*, e1002107. https://doi.org/10.1371/journal.pcbi.1002107.
94. Hallermann, S., de Kock, C.P.J., Stuart, G.J., and Kole, M.H.P. (2012). State and location dependence of action potential metabolic cost in cortical pyramidal neurons. Nat. Neurosci. *15*, 1007–1014. https://doi.org/10.1038/nn.3132.
95. McLelland, D., Baker, P.M., Ahmed, B., Kohn, A., and Bair, W. (2015). Mechanisms for Rapid Adaptive Control of Motion Processing in Macaque Visual Cortex. J. Neurosci. *35*, 10268–10280. https://doi.org/10.1523/JNEUROSCI.1418-11.2015.
96. Kiani, R., Esteky, H., Mirpour, K., and Tanaka, K. (2007). Object category structure in response patterns of neuronal population in monkey inferior temporal cortex. J. Neurophysiol. *97*, 4296–4309. https://doi.org/10.1152/jn.00024.2007.
97. Mazer, J. (2013). Pype2. https://github.com/mazerj/pype2.
98. Yu, H., Lyu, H., Xu, Y., Windolf, C., Lee, E.K., Yang, F., Shelton, A.M., Winter, O.; International Brain Laboratory, and Dyer, E.L., et al. (2024). In vivo cell-type and brain region classification via multimodal contrastive learning. Preprint at bioRxiv. https://doi.org/10.1101/2024.11.05.622159.
99. Radford, A., Kim, J.W., Hallacy, C., Ramesh, A., Goh, G., Agarwal, S., Sastry, G., Askell, A., Mishkin, P., Clark, J., et al. (2021). Learning transferable visual models From natural language supervision. Preprint at arXiv. https://doi.org/10.48550/arXiv.2103.00020.
100. Stuart, G.J., and Spruston, N. (2015). Dendritic integration: 60 years of progress. Nat. Neurosci. *18*, 1713–1721. https://doi.org/10.1038/nn.4157.
101. Tremblay, R., Lee, S., and Rudy, B. (2016). GABAergic Interneurons in the Neocortex: From Cellular Properties to Circuits. Neuron *91*, 260–292. https://doi.org/10.1016/j.neuron.2016.06.033.

STAR★METHODS

KEY RESOURCES TABLE

REAGENT or RESOURCE	SOURCE	IDENTIFIER
Chemicals, peptides, and recombinant proteins		
Muscimol	Tocris Bioscience	Cat# 0289
CM-Dil (red lipophilic dye)	Invitrogen/Thermo Fisher	Cat# V22888
Kwik-Cast silicone sealant	World Precision Instruments	Cat# KWIK-CAST
Dowsil 3-4680 dura gel	Dow Chemical	Cat# 3-4680
Metabond	Parkell	Cat# S380
Deposited data		
Spatiotemporal waveforms dataset	This paper	https://doi.org/10.6084/m9.figshare.19493588
NP Ultra dataset with imposed motion	This paper	https://dandiarchive.org/dandiset/000957
Waveform browser	This paper	https://npultra.steinmetzlab.net/
Experimental models: Organisms/strains		
Mouse: Sst-IRES-Cre	The Jackson Laboratory	JAX Stock #013044; RRID: IMSR_JAX:013044
Mouse: Vip-IRES-Cre	The Jackson Laboratory	JAX Stock #010908; RRID: IMSR_JAX:010908
Mouse: Pvalb-IRES-Cre	The Jackson Laboratory	JAX Stock #017320; RRID: IMSR_JAX:017320
Mouse: Sim1-Cre	The Jackson Laboratory	JAX Stock #006395; RRID: IMSR_JAX:006395
Mouse: Rbp4-Cre	MMRRC Stock	MMRRC Stock #031125-UCD; RRID: MMRRC_031125-UCD
Mouse: VGAT-ChR2-EYFP	The Jackson Laboratory	JAX Stock #014548; RRID: IMSR_JAX:014548
Mouse: Ai32 (RCL-ChR2(H134R)/EYFP)	The Jackson Laboratory	JAX Stock #012569; RRID: IMSR_JAX:012569
Software and algorithms		
Kilosort 2.0	Pachitariu et al.[82]	https://github.com/MouseLand/Kilosort
Kilosort 2.5	Steinmetz et al.[3]	https://github.com/MouseLand/Kilosort
DARTsort	Boussard et al.[41]	https://github.com/cwindolf/dartsort
NEMO (Neuronal Embeddings via MultimOdal contrastive learning)	Yu et al.[55]	https://ibl-nemo.github.io/
Other		
Neuropixels Ultra probes	IMEC	Available at https://www.neuropixels.org/specialty-products as "Neuropixels 1.0 HD"
Neuropixels 1.0 probes	IMEC	Available at https://www.neuropixels.org/

EXPERIMENTAL MODEL AND STUDY PARTICIPANT DETAILS

All experimental protocols were conducted according to US National Institutes of Health guidelines for animal research and approved by the Institutional Animal Care and Use Committee at the University of Washington.For awake, head-fixed acute recordings, wild type C57BL/6 mice of both sexes, between 2 and 8 months of age, were first implanted with custom-made steel headplates and 3D-printed plastic recording chambers. Following recovery, mice were acclimated to head-fixation for at least two sessions before recording. Head-fixation mice were seated on a plastic body restraint tube with forepaws on a rotating rubber wheel. All other animal uses are described separately in individual sections.

METHOD DETAILS

Probe noise model

When using neural probes with planar microelectrodes, the quality of the neural recording (e.g. signal to noise ratio) will depend on several factors, including the electrode size; the electrode impedance and the input impedance of the recording amplifier; the electrode noise and the noise of the recording amplifier; and finally the distance and alignment between the neuron and the electrode. These factors contribute to different signal-degradation effects that are explained as follows.

Signal attenuation due to electrode impedance

The electrode impedance is inversely proportional to the electrode size. Small electrodes can exhibit larger signal attenuation due to the impedance ratio (i.e. voltage divider) at the input of the amplifier. This attenuation is given by: Z_{elec}/Z_{amp}. In the Neuropixels 1.0 design, Z_{amp} corresponds to 27.2 MΩ (at 1 kHz). Thus, the signal attenuation can be calculated as:

Signal attenuation

	Neuropixels 1.0 and 2.0	Neuropixels Ultra	Notes
Electrode area	144 μm^2	25 μm^2	
Z_{elec}	∼100 kΩ	500 kΩ*	*estimated from test structures
Z_{amp}	27.2 MΩ	27.2 MΩ	
Z_{elec}/Z_{amp} * 100%	0.4%	1.8%	

Estimated signal attenuation of Neuropixels probes, Figure 1 and STAR Methods section probe noise model.

Although the signal attenuation is increased by almost 5 times, it continues to be negligible due to the much higher input impedance of the recording amplifier (see above table).

Noise performance

The total noise affecting neural recording has two components: i) the thermal noise generated by the electrode-tissue interface ($V_{n\text{-}elec}$) and ii) the noise of the readout electronics ($V_{n\text{-}amp}$). The total noise can be calculated as:

$$V_{n-total} = \sqrt{V_{n-elec}^2 + V_{n-amp}^2}$$

The noise generated by the electrode-tissue (or electrode-electrolyte) mostly depends on the electrode area, the double-layer capacitance formed at the electrode-electrolyte interface (i.e. electrode impedance) and the resistivity of the saline solution, medium or tissue.[39,46,83]

In the Neuropixels 1.0 design, Vn-amp corresponds to 5.4 µVrms (for the action potential band: 300 Hz to 10 kHz). For the low-impedance TiN electrodes, the electrode noise was modeled and measured in saline as 2.7 µVrms. Based on estimated electrode impedance values, it is possible to predict the noise performance of smaller electrodes for different solution/tissue resistivities.[39] In saline, the total noise can be calculated as in the below table.

Saline noise

	Neuropixels 1.0	Neuropixels Ultra	Notes
Electrode area	144 μm^2	25 μm^2	
Z_{elec}	∼100 kΩ	500 kΩ*	*estimated from test structures
$V_{n\text{-}elec}$	2.7 μV_{rms}	5 μV_{rms}**	**modeled based on estimated impedance
$V_{n\text{-}amp}$	5.4 μV_{rms}	5.4 μV_{rms}	
$V_{n\text{-}total}$	6 μV_{rms}	7.4 μV_{rms}	

Estimated noise of Neuropixels probes in saline, related to Figure 1 and STAR Methods section probe noise model.

If we consider the resistivity of the brain tissue, which is at least 4 times higher than the resistivity of saline, the total noise can be calculated as in the brain noise.

Brain noise

	Neuropixels 1.0	Neuropixels Ultra	Notes
Electrode area	144 μm^2	25 μm^2	
Z_{elec}	∼100 kΩ	500 kΩ*	*estimated from test structures

(*Continued on next page*)

Continued

	Neuropixels 1.0	Neuropixels Ultra	Notes
$V_{n\text{-}elec}$	4.6 μV_{rms}	7.6 μV_{rms}**	**modeled based on estimated impedance
$V_{n\text{-}amp}$	5.4 μV_{rms}	5.4 μV_{rms}	
$V_{n\text{-}total}$	7.1 μV_{rms}	9.4 μV_{rms}	

Estimated noise of Neuropixels probes in the brain, related to Figure 1 and STAR Methods section probe noise model.

Note that in Neuropixels 1.0, the noise is dominated by the readout-electronics noise, while in Neuropixels-Ultra the electrode noise has a bigger impact on the total noise.

Although the electrode noise increases by a factor of ~2, the increase of the total recording noise is only 23% in saline or 32% in brain tissue. This increase is modest relative to the amplitude of ‘biological’ noise (i.e. spiking activity of distant neurons). This indicates that, thanks to the low-impedance of the TiN electrode material, the reduction in electrode size does not significantly impact the quality of the recordings.

Noise and gain characterization

In vitro noise measurements are performed in the standard self-referenced configuration as described in the Neuropixels manual, with the reference and ground connected together and to a Pt wire electrode in the saline bath. Noise on each channel is measured by averaging Fourier power spectra from 5x 3-s-long sections of data, and estimating rms from the integral over 300–10,000 Hz:

$$rms = \sqrt{P * binwidth} = \sqrt{P * \frac{fs}{N_{FFT}}}$$

Where P is the sum over the frequency range in the power spectrum, F_s is the sampling frequency, and N_{FFT} is the number of points in the FFT calculation.

Noise is estimated from *in vivo* data for “low activity” channels with event rates < 0.01 Hz using (1.4826*median absolute deviation). For the gain measurement, the probe ground and reference are connected to the Faraday cage ground, and a 2 mV, 3 kHz sine wave is applied to the saline bath through a Pt wire electrode. The amplitude of the sine wave on each channel is measured by averaging over a 15 Hz window about the 3 kHz peak in the Fourier power spectrum.

Crosstalk estimation

To estimate the crosstalk between channels, we took advantage of our *in vivo* recordings which provide a situation in which a small voltage source is located immediately adjacent to the probe. We reasoned that for neurons with spatially restricted extracellular action potentials, distant sites on the probe should not reflect the waveform of the neuron unless by crosstalk. To the extent that this assumption might not be true (i.e. distant sites really do detect the actual extracellular action potential), we would measure signal at the distant site and incorrectly attribute it to crosstalk; therefore, this estimation strategy produces an upper bound on the true amount of crosstalk.

Specifically, we selected units for which at most 20 sites had significant amplitude of the average waveform (defined as peak-trough amplitude > 25% of the amplitude on the peak site), and averaged the amplitude at the 10 most physically distant sites relative to the peak site. The amplitude on the distant sites was calculated using the same peak and trough timepoints as the peak channel, since any crosstalk should be temporally instantaneous. We report the ratio between this average amplitude on the distant 10 sites and the amplitude on the peak site. This measurement was subject to biological noise, but across an average of n=519 small neurons, we measured 0.0007% ± 0.0736% (mean ± SEM; Figure S4).

Light artifact tests

We tested the sensitivity of NP Ultra probes to 470 nm light (the wavelength used for channelrhodopsin activation). We used a fiber-coupled laser (200 μm core fiber) to shine light directly on probes submerged in phosphate-buffered saline. Light was incident on the front side of the probes. During the tests, we simultaneously recorded from two NP Ultra probes (passive, non-switchable version) and one NP 1.0 probe to compare light artifacts across probe variants. Two different stimulation waveforms were tested (10 ms pulse and 1 s raised cosine stimulus) at three light intensities (0.5, 4.0, 10.0 mW/mm^2). We quantified photo-artifacts in both the spike (0.3-10 kHz) and LFP bands (0.5-500 Hz) by computing trial-averaged photo-evoked responses (100 trials) time-locked to the start of photo-stimulation (Figure S1). Artifact magnitudes were computed as the absolute value of the light-evoked voltage deflection peak during the photo-stimulation period.

Recordings from diverse brain regions in the mouse

At UW

Three iPad screens were positioned around the mouse at right angles. On or before the first day of recording, a 1-2 mm diameter craniotomy with intact dura was prepared with a dental drill over the target brain area under anesthesia. The craniotomy was either protected with removable silicone sealant (Kwik-Cast, World Precision Instrument) or covered with transparent dura-gel (Dowsil 3-4680) with a further protective plastic cap sitting on top of the recording chamber, after the surgery and before recording procedure starts. After several hours of recovery, mice were head-fixed in the recording setup. We used single-ended configuration for all recordings, with ground and reference pins on the probe tied together. We used either external or internal reference methods. For recordings with external referencing, an Ag wire was connected to the probe ground/reference wire and positioned above the skull. After peeling off the silicone sealant, the craniotomy and Ag wire were then submerged in a bath of Ringer's lactate solution. For recordings with internal reference, a probe was directly inserted through the dura gel without solution bath and the reference site on the probe tip was used instead. Prior to each insertion, the electrode shank was coated with CM-Dil (Invitrogen), a red lipophilic dye, for later histological reconstruction of probe tracks.

To sample waveforms from diverse brain areas in a single penetration, we automated the advancement of probes through manipulators (Sensapex Inc., uMP-4) using the Sensapex API via Matlab, following every 5 min of stable recordings. For each step, we advanced the probe by 300 μm at 5 μm/s speed, followed by 50 μm retraction, to help reduce the tissue compression caused by the probe. Recordings normally stabilized within 1 min after probe motion, as visualized by post-processing drift maps. We typically repeated this for 8-16 steps from the surface of the penetration, depending on the final depth of target brain area. For most sessions, we recorded with two probes simultaneously on two hemispheres in a single session.

After recording, mice were perfused with 4% paraformaldehyde. The brain was extracted and then fixed in 4% paraformaldehyde for a further 24 h at least at 4°C. We cleared the brain tissue with iDISCO before 3D imaging with lightsheet microscopy (UltraMicroscope II, LaVision BioTeC). We used 561 nm channel for imaging probe track with Dil and 488 nm channel for brain autofluorescence, with 10 μm isotropic resolution. We registered the imaging volume to Allen Mouse Brain Common Coordinate Frameworks (CCF) Atlas with ARA tools (https://github.com/SainsburyWellcomeCentre/ara_tools), which calls Elastix via a Matlab wrapper. Probe tracks were traced in the atlas-registered brain volume with open-source package Lasagna (https://github.com/SainsburyWellcomeCentre/lasagna). While the Dil track provides a good estimate of the probe trajectory, the depth information between Dil track and electrophysiological recordings usually do not match with high precision, due to the warping and shrinkage of the brain sample during perfusion and tissue clearing steps, and due to uncertainty about the final probe tip location along the track. Therefore, we used multiple electrophysiological landmarks (e.g., cortical layer 5 neuron layer, CA1 pyramidal layer, white matter boundaries, etc) to match the recording sites with the probe trajectory by linear interpolation.[4] After this manual curation process, we assigned each probe site and therefore each spike cluster to designated CCF coordinates.

The NP Ultra brain-wide data was sorted with Kilosort 2.0,[82] using a 96 site template. The timing of all recording epochs were extracted from a manipulator motion start/stop channel synchronized to the electrophysiology data. The first minute of the recording after manipulator motion was discarded due to probe-tissue motion, leaving 4 min of stable recording data for each epoch. Kilosort was then batch run based on epoch timing, and units were selected with an automated quality metric within Kilosort 2.0 after spike sorting.

At Janelia

Acute recordings were conducted at the HHMI Janelia Research Campus, following guidelines set by the Institutional Animal Care and Use Committee. Three male VGAT-ChR2-EYFP mice, aged 6 months, underwent a brief stereotaxic surgery to implant a titanium headpost and build a recording chamber using dental cement for acute head-fixed recordings. Postoperative analgesia was provided using Buprenorphine (0.1 mg/kg, intraperitoneal injection), and Ketoprofen (5 mg/kg, subcutaneous injection) was used at the time of surgery and postoperatively for 2 days. Following surgery, mice were habituated under head restraint in the recording setup for 2 days with incremental acclimatization duration (30 min to 1 h).

On the first day of recording, two to four craniotomies of diameter 1-1.5mm were made with a dental drill over the target areas of interest under anesthesia, while leaving the dura intact. The craniotomies were protected with removable silicone sealant (Kwik-Cast, World Precision Instrument) sitting on top of the recording chamber between recording sessions. After a 3-h recovery period, the animal was head-fixed in the recording setup, and two or four NP Ultra probes were inserted into separate craniotomies and to the target depths, inferred from manipulator readings. The insertions covered brain regions such as the cortex, striatum, thalamus, midbrain, cerebellum, and medulla. The tip of the electrode was coated with CM-Dil (Invitrogen), a red fixable lipophilic dye, before each insertion to enable histological reconstruction of probe tracks. Probes were slowly lowered at a speed of 10 μm/s to the first intended depth using micromanipulators (uMP-4, Sensapex, Inc), and after reaching the desired depth, the inserted probes were allowed to settle for approximately 5 min before recording commenced. Multiple probes were recorded simultaneously for 20-30 min. Since the NP Ultra sites span a length of 288 μm only, after each recording, probes were further inserted by 300 μm to make a successive recording. As such, over the course of a session, probes were advanced 2-6 times to collect data at multiple depths from each penetration, and brain tissue was allowed to relax for a few minutes after each probe advancement. All probes had a wire soldered onto the reference pad, which was shorted to the ground pad. This wire was then connected to an Ag/AgCl wire positioned above the skull. During recordings, the craniotomies and reference wire were submerged in cortex buffer (NaCl 125 mM, KCl 5 mM, Glucose 10 mM, HEPES 10 mM, $CaCl_2$ 2 mM, $MgSO_4$ 2 mM, pH 7.4). Daily recording sessions lasted approximately 2 h and were repeated for multiple consecutive days in a craniotomy, with each penetration separated by at least 200 μm at the point of entry. All recordings were made with open-source software SpikeGLX (http://billkarsh.github.io/SpikeGLX/) in external or tip reference mode, and the animal was awake and sitting quietly in a body restraint tube throughout the recording sessions. The dataset was sorted offline with Kilosort 2.0 using a 96 site template.

To visualize the recording locations, the mice were perfused transcardially with PBS followed by 4% PFA, and their brains were fixed overnight and then cleared with SPiB solution using an aqueous-based clearing method called 'Uniclear' to facilitate whole-brain dilapidation and refractive index matching.[84] The cleared brains were then imaged with a light sheet microscope (Zeiss Z1) using a 5x objective with a voxel size of 1.2 x 1.2 x 6 μm. Whole-brain autofluorescence was captured with a 488 nm channel, while DiI tracks were imaged with a 561 nm channel. The resulting tiled images were stitched together using IMARIS software, and the entire brain stacks were registered to the Allen Institute Common Coordinate Framework (CCFv3) of the mouse brain based on anatomical landmarks, allowing each spike cluster to be assigned to a specific CCF coordinate.

Data was preprocessed using CatGT (https://billkarsh.github.io/SpikeGLX/#catgt) for multiplex correction, filtering, artifact removal, and common average subtraction. Spike sorting was performed with Kilosort 2.0, followed by manual curation. We classify units as either 'unimodal' or 'overlapped'. Unimodal units have distributions in feature space visually that appear to come from a single distribution that does not overlap other units, and refractory period violations are low. 'Overlapped' units have distributions in feature space that overlap other units, and generally have higher refractory period violations. In the analysis of signal and physical distance, all units with > 500 spikes are included, to provide as complete a picture of the activity as possible. For the waveform shape analysis, only 'unimodal' units are included, so that mean waveforms are as close as possible to single units.

At University College London

All experimental procedures were carried out under license from the UK Home Office in accordance with the UK Animals (Scientific Procedures) Act (1986). Acute recordings were performed on adult (>P60) Rbp4-Cre male and female mice kept on a 12 h dark/light cycle. At the time of surgery, mice were subcutaneously injected with Rimadyl (5mg/ml) and Lidocaine (5mg/ml) to numb the area above the skull prior to headplate implantation. A 0.5 g customized metal headplate was attached to the skull using super glue and dental acrylic (Super bond C&B polymer mixed with Super bond monomer and catalyst). After headplate implantation, mice were allowed to recover at 37°C inside an incubator and were closely monitored for 5 days post-surgery. On the first day of recording, mice were administered dexamethasone (Dexadreson, 2 mg/ml, intramuscular injection) to reduce brain swelling. On the first day of recording, one 2 mm-diameter craniotomy was made over the region of interest under anesthesia using a surgical motorized drill. The skull flap was carefully removed to leave the dura mater intact and the exposed brain surface was cleaned using IVE and subsequently protected with transparent Duragel and removable silicone sealant (Kwik-Cast, World Precision Instrument) placed on top of the recording chamber. Finally, the animal was allowed to recover for 3 h before starting any further experimental procedure.

Before recording sessions, mice were acclimated to the experimental rig for at least 3 days: animals were head-fixed above a static 3D-printed holder using a head bar clamp, and habituated to head restraint of increasing duration (starting from 10 min and up to 1 h). On recording days, the shank of Neuropixels probes was covered with red fluorescent dye DiI (Invitrogen) to allow for histological probe tracing. Then the probe was inserted perpendicularly to the cortical surface using a micromanipulator (Sensapex uMP-4). Probe insertion speed was kept at 20 μm/s to minimize cortical damage, terminating at 2,000-2,800 μm below the brain surface for NP 1.0 and 1,200 μm for NP Ultra. Probes were allowed to settle for about 10 min before the start of every recording. All recordings were carried out using the acquisition software SpikeGLX (http://billkarsh.github.io/SpikeGLX/) using tip reference mode, and lasting about 1.5-2 h. Every animal was recorded for a maximum of three consecutive days, with recordings taking place at different locations within the craniotomy.

All recordings were processed to align channel sampling using the common average referencing software CatGT (https://billkarsh.github.io/SpikeGLX/#catgt); putative neuronal units were spike sorted with Kilosort 2.0 (https://github.com/MouseLand/Kilosort2) and Phy2 (https://github.com/cortex-lab/phy), and manually curated in Phy2. For every unit, we computed spike-triggered voltage maps showing the extracellular signature of each action potential across time and channels. We then averaged 2,000 of these maps to compute a template spike voltage map for each unit. We located the putative soma as the channel with the largest sink recorded at the time of spike in the template maps.

To correct for vertical probe motion during the recording we used a two-step strategy. First, we used Kilosort 3.0 drift estimation to correct for slow probe movements at the second scale. Second, to correct for fast movements on a spike-by-spike basis, we used 1D cross correlation to compute the vertical shifts needed to register spike-triggered voltage maps to a target reference map obtained from 1,000 long-ISI spikes selected randomly throughout the recording.

To identify units with significant dendritic back-propagation, e.g. those for which the apical dendrite was best aligned with the probe, we used a permutation test. Starting from the soma, we compared the average spike amplitude of every channel in the template spike map to a null distribution of amplitudes obtained from 500 shuffled template maps, each computed from a random linear shift of the spike times. Moving from towards the cortical surface, we considered as significant dendritic recordings those channels bearing signals larger than 95th percentile of the null distribution. We included for further analysis neurons which displayed significant dendritic back-propagating signals extending beyond 250 μm from the soma.

Muscimol experiments

To verify the identities of small footprint waveforms in the mouse cortex, we topically administered muscimol to the surface of the dura through the craniotomy, while acutely recording cortical activity with NP ultra probes in head-fixed mice. Acting as a GABA agonist, muscimol will silence neural activity of local cortical neurons, but leaving activity of long range axons from elsewhere intact.

Headplate implant surgery, craniotomy surgery and acute NP ultra recordings were performed mostly as described in the STAR Methods section "recording from diverse brain regions in the mouse (At UW)" section, with additional details as below. During the craniotomy surgery procedure, a cement well was built around the craniotomy after the craniotomy was made and covered with removable silicone sealant, to constrain the spatial spread of drug application within the craniotomy during recording. For acute NP ultra recordings, the craniotomy was submerged in a bath of Ringer's lactate solution during control conditions. After a period of baseline spontaneous activity recording for around 10 min, a set of 5-min sparse noise stimuli were presented on the iPad screens for receptive field mapping.Thereafter, 5mM muscimol in Ringer's solution was applied to the craniotomy and "bathed" the surface of the brain for the remainder duration of the recording. The majority of unit activity were silenced, 3–10 min after the muscimol application. A second set of 5-min sparse noise stimuli were then presented for receptive field mapping for units that survived muscimol.

Spike sorting methods

To take advantage of the high spatial resolution of NP Ultra sites, we utilize a spike sorting pipeline, DARTsort,[41] that takes advantage of recent progress in spatial localization of spikes. After an initial detection step, we denoise[85] and localize the spikes.[42]

Localization is obtained in 3D by modeling the source of spikes as a point-source of brightness a and location (x,y,z) and solving for (a,x,y,z) by minimizing the L2 loss between the observed spike amplitudes on all channels and the point-source reconstructed amplitude. We then estimate the motion of the probe (i.e., drift) relative to the recorded neurons. For this registration step we use the decentralized approach,[43] which is more robust to boundary effects (i.e., neurons moving on or off of the short NP Ultra probe) than the template-based registration method used in Kilosort2.5.[43] After registration, we have a robust estimate of each spike's amplitude and position relative to the probe. Then, by subtracting the estimated drift from the position of each spike, we obtain a set of 3D features for each unit: registered 2D position (taking only the 'x' and 'z' coordinates across the face of the probe from the full fit 3D position) and spike amplitude.[86] We cluster in this 3D feature space using HDBSCAN,[87] and then recursively re-split these clusters using additional features computed by principal components analysis applied within each cluster.[88] Even after registration, we find that some units have some remaining drift (changes in mean registered location and amplitude) over time. Therefore we divide the recording into 5-min segments that we separately cluster and then merge, to make the clustering step more robust to these individual-unit drift effects.

Next we run a template-matching deconvolution step to resolve "collided" spikes that overlap temporally and spatially. To enable drift-aware template matching, we construct a set of denoised "super-resolution" templates for each unit by dividing the depth of the probe into 2 μm bins and then averaging the spikes localized to each bin separately. During template matching, we can then shift these super-resolved templates according to the drift to efficiently detect spikes for each unit. One major benefit of this approach is that we do not need to apply a shift/interpolation step to the raw data (as in Kilosort 2.5); in practice, we found that this raw-data interpolation removed signal near the edge of the probe due to boundary effects, which are particularly problematic for the small dense NP Ultra probes. In our approach, instead of shifting the raw data, we shift the templates, allowing us to robustly track neurons moving on or off the probe.

As the initial clustering is usually imperfect, we perform the above steps iteratively: cluster, then deconvolve, then re-cluster on the deconvolution output. We use the post-deconvolution collision-subtraction method[85] to denoise the spikes obtained in the deconvolution step, to enable improved iterative clustering.

Methods for site pattern comparison using spatial resampling

We resampled data recorded with NP Ultra to predict what signals would have been recorded from the same brain location and time period with a lower density probe. To do this, we simply average together the four 5x5 μm NP Ultra sites that are co-localized with a single 12x12 μm site in the resampled pattern (Figure 2E; due to the 1 μm gaps between sites in NP Ultra, the four 5x5 sites fill the 12x12 μm area almost exactly, with small missing gaps). In each case, a single 12x12 μm simulated recording site is obtained by averaging across four 5x5 μm recording sites of NP Ultra, recapitulating the way that recording sites average signals over the extracellular space that they span.[23,89,90] We used this method to measure the expected changes in amplitude and waveform shape for the Neuropixels 1.0 and 2.0 patterns, and a "large dense" pattern of 12x12 μm sites with 12 μm pitch (Figures 2G–2K, 3D–3G, 7D, and 7F).

For measurements of the site size and pattern dependence that include the effects of noise - specifically, for computing the 'Template SNR' (Figure 2I) and for analyses involving spike sorting the resampled raw data (Figures 3D–3G) - we needed to create data with realistic noise and waveform variation, which in real data combines electronic noise with signals from distant units. Averaging the four raw traces together as described above reduces the noise by $1/\sqrt{2}$; to boost the noise back to normal levels, simulated noise with a matched frequency spectrum is added to the averaged traces (code at: https://github.com/jenniferColonell/NP_Ultra_downsample).

An interpolation method was used for the analyses on waveform shape and peak amplitude in Figures S4 and S5. The mean waveform from the Ultra data was used to create a gridded interpolant (MATLAB, using 'makima' interpolation). The waveforms for an arbitrary pattern with any site size and position can then be estimated by averaging together interpolated waveforms at sets of points that span the model sites. This method has the advantage of allowing a test site pattern that is slightly better matched to the true NP 1.0 and NP 2.0 geometry than in Figure 2E.

Analyses of sorting quality

Spike amplitude was calculated as peak-to-peak voltage, i.e. the maximum voltage of the waveform minus the minimum (Figures 2G, 2H, S4A, and S5A).

In template matching methods, a multi-site template is convolved with the filtered data to detect spikes. To quantify the impact of site density on detectability in template matching, we calculate the 'Template Matching Signal to Noise Ratio' for each unit (Figures 2I, S4B, and S5B) defined as:

$$TM - SNR = \frac{\sum_{s}(T \cdot V_s)}{N \cdot std(T \cdot V_R)}$$

Where T is the template vector of 40 time samples * number of sites in the template, and V is measured voltage on those sites centered either at a spike time (to measure signal) or a randomly chosen time (to measure noise). S indexes spike times of the unit, R indexes random times, and N is the spike count of the unit. This is an estimate of the signal to noise ratio in data filtered by the template. Spike times for each unit are drawn from the sorted Ultra data, and the TM-SNR is calculated for the Ultra data and spatially resampled data obtained from averaging sites (see exact patterns in Figure 2E).

The spatial spread of spikes was calculated as the standard deviation of the x-coordinates (lateral dimension, across the face of the probe) or of the z-coordinates (axial dimension, down the length of the probe) across all spikes in a given unit (Figures 2J and 2K). For the resampled patterns, these coordinates were computed by resampling each spike individually and then computing that spike's estimated coordinates using the same method employed in the main DARTsort pipeline.

To understand the possible effects of this spatial scatter in more detail, we computed the average distances between neurons, as well as the minimum distance that each site pattern should be able to resolve, in a simple simulation (Figures S4C and S5C). We use a Monte Carlo model to generate sets of peak-to-peak voltages over sites for a point source with 1/R amplitude falloff, placed 15 μm from the probe, with peak amplitude at the probe of 50 μV and rms noise of 14 μV. For each set, all sites within 60 μm of the peak site are fit to obtain an estimated XZ position.[42] Modeled noise in the position estimate is the standard deviation of the Monte Carlo trials, and is 5 μm for a NP Ultra probe, and 25 μm for the NP 2.0 pattern. The increased accuracy is due to the inclusion of more sites in the 60 μm radius of fit points, which decreases the impact of noise. These values are the upper limit of position resolution, and can be compared to the measured distribution of nearest neighbor unit distances from the Ultra data. Units with nearest neighbor distances below the spatial resolution of the probe will be more difficult to sort. The experimental nearest neighbor distributions are calculated including both 'unimodal' and 'overlapped' units to build as complete a set as possible to assess the potential impact of this difference in spatial resolution on sorting. Note that standard deviations of positions in experimental data can be larger (see Figures 2J and 2K); this is likely due to variability in the spikes (background firing, incomplete drift correction) not captured in the simple model.

To measure how more detailed spatio-temporal waveforms could affect sorting, we created a waveform distance metric and compared the waveform distances measured at varying site density (Figures S4D and S5D). Higher site density will always provide more detail, and better confirmation of small differences, but the engineering question is whether the waveforms are 'mostly' smoothly varying and distinguishable with sparse sampling. To isolate the waveform distance from difference in z position and amplitude, a neighborhood of rows centered about the peak row is taken for each template, and the amplitude is normalized. For the spatially resampled patterns, the expected waveforms are calculated using interpolation of the full density waveform, with the sparser pattern centered at the position of the peak row for each template. Centering the sparse pattern on the peak row ensures the two templates look as similar as possible, by ensuring that the same part of the footprint is sampled.

A simple metric to compare the two normalized templates [A,B] is the L1 norm of the difference between the two divided by the sum of the L1 norm of both waveforms, summed over sites, that is:

$$multi\ site\ L1 = \frac{\sum_{sites} L1(A - B)}{\sum_{sites}(L1(A) + L1(B))}$$

This quantity is essentially the fraction of detected signal that is different between the two templates. It is a characterization of the waveform shape that does not account for noise in individual spikes.

Yield, decoding, and stability testing with imposed probe-brain motion

Recordings

To make recordings with imposed probe motion in head-fixed mice (n = 2 mice, n = 6 sessions), we automated the probe motion through manipulators (Sensapex Inc., uMP-4) using the Sensapex API via Matlab. Manipulators were programmed to alternate between moving forward and backward along the probe axis, for a total of 10 steps forward and 9 alternating steps backwards with 25 μm travel in each direction at 1 μm/s speed, which results in 25 μm net total forward displacement disposition of the probe by the end of imposed motion. A digital synchronization signal was issued at the start and end of each motion step for later alignment with neural data. To match neuron identities before and after imposed motion, a battery of 118 natural images with 60 repetitions per image were presented to 'fingerprint' visual responses. Images were presented in a random order. An average of 30 repetitions of the image set were presented before imposed motion, and an average of 15 repetitions were presented after imposed motion. The duration of each image follows a randomized exponential distribution (mean: 0.5 s; minimum: 0.2 s; maximum: 3 s). NP Ultra probes were inserted into the visual cortex at 700-900 μm depth to sample deep layer neurons.

The NP Ultra imposed motion dataset was spike-sorted with DARTsort (see "spike sorting methods").[41] The original full pattern data, as well as the same data resampled to NP 1.0-like, NP 2.0-like, and 12 μm large dense site patterns (see "methods for pattern comparison using spatial resampling" and Figure 2E), were sorted. The timing of imposed motion epochs was extracted from a manipulator motion start/stop channel synchronized to the electrophysiology data.

Yield and stability analysis

To assess and compare the yield and tracking stability of recorded neurons across different channel densities (full density NP ultra, NP 1.0-like, NP 2.0-like, and 12 μm large dense), visual response fingerprints were created for each unit by concatenating average PSTHs (window 0 to +250 ms aligned to image onset, bin size 10 ms) for all 118 images into a single vector. PSTHs were normalized for a given unit by subtracting its baseline activity (-100 to 0 ms) averaged across trials prior to image onset. PSTHs were denoised by reconstructing each PSTH from the top two principal components taken on the average PSTH per image x time points matrix for each unit (dimensions 118x35).

To determine whether a unit had a reliable visual fingerprint, a null distribution for each unit was created by randomly permuting the image identities before concatenating the PSTHs into a vector (Figures 3B and S7A). This distribution preserves the noise and average PSTH time-course of a given unit while disrupting its selective visual response fingerprint. Average PSTHs were calculated from odd-numbered pre-motion trials and even-numbered pre-motion trials. Image identities were randomly permuted 1,000 times, and odd-numbered pre-motion trials were used to create the null distribution. Units were considered to have a reliable visual response if their original correlation score (i.e. pre-motion odd vs. pre-motion even trials) was greater than all scores in their null distribution (i.e. 1,000 pre-motion odd shuffles vs. pre-motion even trials). This ensures that included neurons have both a reliable fingerprint (i.e. responses are consistent between trials of the same image) and a selective fingerprint (i.e. responses to each image significantly vary).

To create a distribution of pre- vs. pre- and pre- vs. post- imposed motion fingerprint correlations (Pearson correlation coefficient), 1000 unique sets of visual fingerprint vectors were constructed for each neuron by randomly partitioning the image repetitions for each image before imposed motion into 2 non-overlapping subsets (15/30 trials in each subset, for all 118 images). In each of these 1000 sets, fingerprints from each pre-motion subset of trials (i.e. the average across trials) were correlated, and the fingerprint from one pre-motion subset was correlated with the fingerprint from the post-motion trials (Figures S7B and S7C). The fingerprint stability ratio for a given neuron was calculated by dividing the mean of the 1,000 pre- vs. post-motion correlations by the mean of the 1000 corresponding pre- vs. pre- correlations. To compare fingerprint stability tracking across the 4 site patterns, stability ratios for every neuron sorted from a given pattern were pooled across all sessions (Figure 3H). Neurons were only included in this analysis if they had a reliable visual response and had a stable firing rate between the pre- and post-motion periods (neurons were dropped if the mean firing rate across all PSTHs in pre-motion period was >4x different than that of the post-motion period).

Image decoding analysis

To assess whether the increased yield of visually responsive neurons captured by NP Ultra corresponded to increased information about visual stimuli, we decoded natural image identities from NP Ultra and compared the performance to decoding from LD, 2.0, and 1.0 patterns. Only visually responsive neurons, i.e. those with a reliable visual fingerprint, were included in the analysis. A minimum of 5 visually responsive neurons per probe was required for inclusion in analysis. Only images displayed before imposed probe motion were included in the analysis.

For each visually responsive neuron, we constructed PSTHs for each trial across all images, using 10 ms bins from -100 to 250 ms relative to stimulus onset. We then performed singular value decomposition (SVD) on the binned PSTH arrays of each neuron (size trials x time bins), retaining the first two principal components to obtain a low-dimensional representation of each neuron's activity pattern. These per-neuron components were concatenated to form a population representation of image PSTH responses. A second SVD was then applied to this population representation, and a maximum of 15 dimensions were retained as predictors for decoding (fewer than 15 dimensions if there were 7 or fewer visually responsive neurons available).

Rather than attempting to classify all 118 images simultaneously, we employed a pairwise decoding strategy. For each possible pair of images (6,903 unique pairs from 118 images), we trained a separate binary classifier. Unregularized Linear Discriminant Analysis (LDA) with diagonal covariance estimation was used as the classification algorithm ("diaglinear" option in MATLAB's fitcdiscr). To address potential class imbalance, observation weights were applied inversely proportional to class frequencies. Decoding accuracy was assessed using 5-fold cross-validation.

The decoding pipeline (SVD dimensionality reduction → LDA on all image pairs) was run multiple times for each probe with increasing numbers of neurons, starting from the minimum of 5 and incrementally adding neurons until reaching the maximum available in each population. When using less than the maximum number, neurons were randomly selected from the pool of visually responsive cells.

We analyzed decoding performance per session and probe type by calculating mean decoding accuracy across all image pairs and across the top 10% most decodable pairs per session and probe (Figure 3F). When analyzing decoding performance as a function of increasing neuron count, a minimum of 3 sessions was required for a given neuron count on a specific probe type to be included in the analysis (Figure 3G). Statistical comparisons between probe types were conducted using paired comparisons (Wilcoxon signed-rank test) between probe types on the same session.

Biophysical simulations

All neural simulations (Figures S3, S10, and S11) were done through LFPy 2.3[91] running on NEURON 8.1.[92] Action potentials were evoked by a step current injection (POINT_PROCESS in NEURON), where the amplitude of the current was adjusted for each cell model to evoke an action potential. Calculations of extracellular potentials were done with LFPy, assuming an electrode diameter of 5 μm, incorporated through the disc-electrode approximation. Simulations in Figure S3 used the rat layer 5 pyramidal cell model.[93] Simulations in Figure S11 used the rat layer 5 pyramidal cell[94] (available from https://modeldb.science/144526), and the parameters for the passive and active conductances for the axon models used in Figure S10 were extracted from the same neuron model.

Recordings from species other than mouse

Recordings from monkey

One macaca nemestrina weighing 6.6 kg (female, 9 yr) participated in the experiments which were conducted in the anesthetized, paralyzed preparation. At the start of the experiment the animal was placed in the stereotaxic instrument and then a craniotomy and a durotomy were performed to target the primary visual cortex (V1). Anesthetic and paralytic regimens are as described elsewhere.[95] All animal procedures conformed to National Institutes of Health guidelines and were approved by the Institutional Animal Care and Use Committee at the University of Washington.

The NP Ultra probe was advanced into the cortex using a hydraulic Microdrive (MO-97A, Narishige) which was mounted onto the stereotaxic arm. Once spike waveforms first appeared on the spikeGLX activity map, we retracted the probe 50 μm and mapped the receptive field (RF) of recorded neurons using achromatic bars under experimenter control. Then data collection on the main experiment began, during which we presented 200 images of naturalistic objects[96] repeatedly (presentation duration: 200 ms). Images were sized to cover mapped RFs.

As the data were continuously collected we completed the following sequence of operations 11 times: (1) probe at rest for 10 min, (2) advance probe 300 μm deeper over a 2 min duration, (3) retract probe for 50 μm. This procedure allowed us to record spike waveforms at 11 different depths where every depth was 250 μm deeper than the previous recording site. Following completion of the recording session, we retracted the probe and confirmed that spikes completely disappeared at a depth within 200 μm from where spikes had first appeared during probe insertion.

Stimuli were presented on a liquid crystal display monitor (24 inches; 100-Hz frame rate; 1920x1080 pixel size, XL2430-B, BENQ) using custom experimental control software, Pype2.[97] Neural data were acquired using spikeGLX with internal tip reference.

The data were batch sorted based on epoch timing, with Kilosort 2.0 using a 96 site template, and units were selected with an automated quality metric within Kilosort 2.0 like recordings from other species.

Recordings from lizard

All experimental procedures were performed in accordance with German animal welfare guidelines: permit no: V54-19c20/15-F126/2006 delivered by the Regierungspraesidiμm Darmstadt (E. Simon).

A day before surgery, the lizard was administered analgesics (butorphanol, 0.5 mg kg^{-1} subcutaneously; meloxicam, 0.2 mg kg^{-1} subcutaneously) and antibiotics (marbofloxacin, marbocyl, 2 mg kg^{-1}). On the day of surgery, anesthesia was initiated with isoflurane in an induction box and maintained with 1–4% isoflurane after intubation (Hallowell EMC anesthesia Workstation AWS). The lizard was placed in a stereotactic apparatus (Kopf 963) after ensuring deep anesthesia (absence of corneal reflex). Body temperature during surgery was maintained at 30°C using a heating pad and esophageal temperature probe (Harvard apparatus part number 50-7213). Heart rate was monitored using an Ultrasonic Doppler flow detector (PARKS medical electronics, INC. model 811-B). The skin covering the skull was disinfected using a 10% povidone-iodine solution before removal with a scalpel. A fine layer of UV-cured glue (Oxford Flow Light Cure Flowable micro-hybrid composite A2) was applied around the exposed surfaces of the skull. A 3×2 mm craniotomy was then drilled around the parietal eye and the pericranium was removed. The parietal eye was retracted and fixed to the posterior edge of the craniotomy using histo-acryl tissue glue. The dura and arachnoid layers covering the forebrain were removed with fine forceps. A silver wire was inserted into the CSF fluid next to the olfactory tract, acting as both reference and ground. Pia was removed over the area of probe insertion (medial cortex). Prior to insertion, the probe was mounted on a movable drive (R2Drive, 3DNeuro), and secured to a stereotactic holder. The probe was stained with DiI (Invitrogen™, Vybrant™ DiI cell labeling solution) and implanted 500 μm deep in the medial cortex (MC) at a speed of around 100 μm/s.

After insertion of the probe, the brain was covered with Duragel (Cambridge Neurotech), and the craniotomy sealed with sterile vaseline. The microdrive base was fixed to the skull with UV glue and the microdrive was released from the stereotactic holder. Finally, a 3D-printed cap was mounted around the skull. The cap provided mechanical protection, carried the head-stage, as well as colored strips of tape for head-direction and position tracking. A silicone sealant (Kwik-Cast, World Precision Instruments) was applied around the edges of the cap and skin. After surgery, the lizard was released from the stereotactic apparatus and left on a heating pad set to 30°C until full recovery from anesthesia. On the days after the surgery, probes were slowly lowered into the tissue (up to 280 μm a day).

During recording sessions, lizards were freely moving in a 150 cm diameter circular arena, with two salient opposing visual cues in a brightly lit room. The room was heated to 29°C, allowing lizards to stay active for an extended duration. Live prey items (mealworms) were dropped into the arena at random times and locations, motivating lizards to explore and maximize arena coverage.

After the end of the experiments, the lizard received intramuscular injections of ketamine and Dormicom, followed by induction and intubation with isoflurane as described in the surgical method. The 3D printed cap, head-stage, and microdrive carrying the probe were retrieved. Lizard was then decapitated and immediately perfused through the carotid arteries with PBS, followed by 4% formaldehyde. The brain was removed and stored in 4% formaldehyde for one day, followed by an additional day in a 30% sucrose solution. The brain was frozen with dry ice and cut into 70 μm coronal slices. Slices were mounted on glass slides, and stained with DAPI. The final position of the tip of the probe was identified based on tissue damage and a DiI signal, imaged using a slide-scanner (Zeiss, Axio scan Z.7). The data were batch sorted with Kilosort 2.0 using a 96 site template, and units were selected with an automated quality metric within Kilosort 2.0 like recordings from other species.

Recordings from electric fish

All experiments adhered to the American Physiological Society's Guiding Principles in the Care and Use of Animals and were approved by the Institutional Animal Care and Use Committee of Columbia University. Weakly electric mormyrid fish (7-12 cm in length) of the species Gnathonemus petersii were used for recordings. Fish were housed in 60 gallon tanks in groups of 5-20. Water conductivity was maintained between 65-100 microsiemens both in the fish's home tanks and during experiments. For surgery to expose the brain for recording, fish were anesthetized (MS:222, 1:25,000) and held against a foam pad. Skin on the dorsal surface of the head was removed and a long-lasting local anesthetic (0.75% Bupivacaine) was applied to the wound margins. A plastic rod was attached to the skull with Metabond (Parkell) to secure the head and a craniotomy was performed over the C1 region of the cerebellum. Gallamine triethiodide (Flaxedil) was given at the end of the surgery (∼20 μg/cm of body length) to immobilize the fish and fresh aerated water was passed over the fish's gills for respiration. The rate of the electric organ discharge motor command was monitored continuously by electrodes positioned near the electric organ in the tail. Electrosensory stimuli were delivered (0.2 ms duration square pulses) between an electrode in the stomach and another positioned near the tail. Probes were inserted vertically into the cerebellum along the midline and lowered slowly (∼10 μm/s) to a final depth of ∼3.5 mm. The data were batch sorted with Kilosort 2.0 using a 96-site template, and units were selected with an automated quality metric within Kilosort 2.0 like recordings from other species.

Brain region abbreviations

MO: Somatomotor areas; ORB: orbital area; VIS: visual areas; PIR: Piriform area; CTXsp: cortical subplate; CA1: hippocampal CA1; SUB: Subiculum; CA3: hippocampal CA3; DG: Dentate gyrus; cc: corpus callosum; VPM: ventral posteromedial nucleus of the thalamus; VPL: Ventral posterolateral nucleus of the thalamus; PO: Posterior complex of the thalamus; CP: Caudoputamen; ACB: Nucleus accumbens; MB: midbrain.

Optotagging

Optotagging experiments

For optotagging experiments, four different transgenic mouse lines were used: 1) Sst-IRES-Cre;Ai32, 2) Vip-IRES-Cre;Ai32, 3) Pvalb-IRES-Cre;Ai32, and 4) Sim1-Cre;Ai32. Ai32 is a reporter line that expresses channelrhodopsin in Cre+ cells. In each experiment we made recordings in parallel from 2-3 NP Ultra probes mounted on separate New Scale Technologies micromanipulators. Electrophysiological signals were acquired with the Open Ephys GUI software as described previously.[7] During the experiment, we recorded sequentially at 3-4 depths within the cortex. Probes were first inserted superficially in the cortex (∼200 μm deep) and allowed to settle for 10 min. We then ran the optogenetic protocol (described below). Next, probes were inserted deeper into the cortex (200-300 μm), allowed an additional 10 min to settle, and the optogenetic protocol was repeated. This process was repeated for up to 4 probe insertion depths. Recordings were made on a single day or on consecutive days from the same mouse. Recordings were spike-sorted with Kilosort2.5 and manually curated for single unit activity.

We used a 470 nm laser to stimulate and optotag neurons expressing Cre and channelrhodopsin in each transgenic mouse line and experiment. For interneuron photostimulation, lasers were coupled to a 200 μm optic fiber. For Sim1-Cre;Ai32 L5 pyramidal neuron photostimulation, the laser path was guided by a pair of galvo-coupled mirrors to focus light to a precise point on the brain surface to minimize recurrent excitation. We used two different photostimulation patterns: a 10 ms square-wave pulse and a 1 s raised cosine ramp. On each trial, light was delivered at one of three light intensities levels (0.2, 4.1, and 10.0 mW/mm^2). These six photostimulation inputs were randomly interleaved, and each was repeated for 100 trials. The average inter-trial interval was 2 s. In total, the photostimulation protocol lasted ∼20 min and recordings were conducted over a total of ∼30 min.

Identification of opto-tagged units

First-pass identification of opto-tagged units used an algorithmic approach to find units of similarly shaped peri-stimulus time histograms (PSTH) during a 1 s raised cosine ramp stimulation at the highest light intensity (see above). This method did not disambiguate between units that were directly stimulated and those that showed an indirect increase in firing rate. Identified units were used as a baseline comparator for further classification.

Unsupervised identification of opto-tagged units in each transgenic mouse line was performed.[38] First, the PSTHs for all stimulation patterns within a given photostimulation intensity were averaged across all trials, then the average PSTH for each pattern and intensity was concatenated, forming a neurons x response-vector matrix. This matrix was then normalized and PCA was applied to reduce the dimensionality of the dataset. All units were then visualized in a low-dimensional space via Uniform Manifold Approximation and Projection (UMAP) using all timeseries PCs. Doing so allowed us to determine whether units with a similar PSTH structure aggregated to the same regions (Figure S16).

Clustering of units was performed using Density-based Spatial Clustering of Applications with Noise (DBSCAN). We chose this method of clustering units as it does not require an *a priori* knowledge of the number of clusters expected and is robust against clusters of varying shapes and sizes, like those produced by UMAP. Hyperparameters for DBSCAN clustering were specific to experiments performed within each transgenic line and were obtained using K-Nearest Neighbors (KNN) to estimate the distance of each data point to the next closest point, then expanding this distance to include the 10th NN. The inflection point in the distribution of these distance values was used as the cluster radius (ε) for DBSCAN. The resulting clusters of units were then compared against those found in our first-pass sorting approach and validated by ensuring a short latency response during a 10 ms square wave pulse photostimulation.

Supervised waveform classification of inhibitory neurons

Neuron features

Feature	Abbreviation	Definition	Units
Amplitude	Amp.	the absolute difference in voltage between the spike minimum (trough) and the post-trough maximum (peak)	μV
Duration	Dur.	the time delay between the trough and post-trough peak	ms
Pre-peak-to-trough ratio	prePTR or pPTR	the ratio between the maximum voltage prior to the trough and the trough	ratio
Peak-to-trough ratio	PTR	the ratio between the maximum voltage after the trough and the trough	ratio
Repolarization slope	Repol. slope	the slope of the linear fit between the trough and 0.3 ms after the trough	mV/ms
Recovery slope	Recov. slope	the slope of the linear fit between the post-trough peak and 0.3 ms after the peak	mV/ms
Average inter-spike interval	Avg. ISI	the average time between spikes calculated across the recording, excluding epochs of photostimulation	s
Baseline firing rate	baseline FR	the average firing rate 1 s prior to photostimulation epochs	spks/s
Spatial footprint	footprint	the radial distance about the peak amplitude channel within which the average amplitude across channels $\leq$30 μV	μm

Features used for cell type classification, related to Figure 7 and STAR Methods section supervised waveform classification of inhibitory neurons.

Linear discriminant analysis

Linear discriminant analysis (LDA, Figure 6H) was performed via its implementation in SciKit-Learn (Python version 3.9.12). Briefly, pairwise comparisons between unit classes proceeded first by randomly subsampling each dataset, without replacement, to the lowest number of units among the unit classes to be compared (PV, n = 238). Only prePTR and PTR single-channel 1D features were used in this analysis. Bootstrapping of the LDA model to subsamples of each unit class over 100 iterations with 100 random initial states and each iteration cross-validated 5-fold. Performance of the model was quantified as how accurately the model classified each unit, given a label matrix. Accuracy scores were averaged across all iterations for each comparison to give a mean classification accuracy score and compared against chance levels of classifying a unit correctly (two classes per comparison, chance = 0.5).

Cross-correlogram analysis for putatively monosynaptically connected neurons

Cross-correlograms were computed between each pair of neurons that included one narrow-spiking small footprint (NS_S) and one other (n > 125,000 pairs, n = 40 recordings) with a 1 ms bin size using all spikes from the recording. Excitatory interactions were identified as those in which the post-reference spike firing rate period increased to greater than five times the pre-spike standard deviation, whereas inhibitory interactions were those in which the firing rate decreased by at least the same amount.

Random forest classification

Validated opto-tagged units and untagged units formed the basis of a label matrix that was then used to classify neuronal types using random forest classification. Because significant differences could be found between RS, NS_L, and NS_S groups (Figures 6E–6G and 7D), these units were included as distinct categories during classification.

Random forest classification was performed via its implementation in SciKit-Learn (Python version 3.9.12) using three different feature sets computed independently on mean electrophysiological waveforms gathered from NP Ultra probes and interpolated, “NP 1.0-like” unit-matched data. These feature sets were 1) 1-dimensional scalar values computed from the peak amplitude channel (Figure 7C; neuron features table) 2) the peak amplitude waveform and 3) All 1D scalar features and spatial footprint.

The process of random forest classification proceeded as the following: NP Ultra data from the entire population of recorded units was spatially resampled to a NP 1.0-like geometry (Figure 2E). Units for which the peak channel amplitude dropped below 50 μV were then removed from both datasets for the purposes of this analysis. Data (NP Ultra and NP 1.0-like) from each unit class category was then randomly subsampled, without replacement, to the lowest number of units among optotagged cell types (SST, 116 units) and pooled. This process was repeated through 100 iterations using 100 initial states. Principal components analysis was then performed on the pooled data for each probe type prior to classification and classifier hyperparameters were then optimized via grid search using 5-fold cross validation. Classification proceeded via 5-fold cross-validation where the classifier was trained on 80% of the input data and performance was evaluated using held-out test data (20%). Classification performance was evaluated as the prediction accuracy of the classifier on left-out data over each bootstrapped iteration. Confusion matrices were computed as the comparison of predicted classes to true classes for each subsampled dataset under 100 random initial states.

Multimodal classification of inhibitory neurons

To improve cell-type classification of the optotagged units, a recently developed multimodal cell-type classification method NEMO (Neuronal Embeddings via MultimOdal contrastive learning) was utilized.[98] NEMO is a multimodal contrastive method based on CLIP[99] that jointly embeds the activity autocorrelations and average extracellular waveforms (templates) of each neuron. By finding a joint representation of different modalities, NEMO is able to extract intrinsic properties of a neuron that are predictive of its cell type.[100,101]

The activity autocorrelations were constructed by creating an autocorrelogram (ACG) image for each neuron. This involved smoothing the spiking activity using a 250-ms boxcar filter, segmenting the firing rate distribution into 10 deciles, and constructing ACGs for each decile. The resulting ACG image effectively represents how a neuron’s autocorrelations vary with its firing rate. By generating ACGs for each decile, this approach captures firing rate-dependent changes in autocorrelations.[36] To eliminate stimulus-induced effects, we excluded spikes occurring within 1,100 ms of each stimulus onset and computed ACG images using only the remaining data. The average waveforms were constructed from approximately 500 recorded waveforms for each neuron. We utilize multi-channel templates which take advantage of the detailed spatial structure enabled by the small channel spacing. We use nine channels with the highest peak-to-peak (ptp) amplitude, re-ordered from highest to lowest amplitude.

NEMO was trained on the activity autocorrelations and average waveforms for all the *untagged* units (8,491 neurons) in a fully self-supervised manner. NEMO was then fine-tuned to classify the *optotagged* units. NEMO was evaluated using 5-fold cross-validation with 10 repeats. By pre-training on untagged units and fine-tuning on the optotagged units, NEMO was able to reach a .80 F1 score and balanced accuracy on classifying inhibitory cell types (the confusion matrix is shown in Figure 7H).